Consistent lattice Boltzmann modeling of low-speed isothermal flows at finite Knudsen numbers in slip-flow regime: Application to plane boundaries

Goncalo Silva* and Viriato Semiao
LAETA, IDMEC, Mechanical Engineering Department, Instituto Superior Tecnico, Universidade de Lisboa, Av. Rovisco Pais 1, 1049-001 Lisbon, Portugal
(Received 17 February 2017; revised manuscript received 2 May 2017; published 18 July 2017)

The first nonequilibrium effect experienced by gaseous flows in contact with solid surfaces is the slip-flow regime. While the classical hydrodynamic description holds valid in bulk, at boundaries the fluid-wall interactions must consider slip. In comparison to the standard no-slip Dirichlet condition, the case of slip formulates as a Robin-type condition for the fluid tangential velocity. This makes its numerical modeling a challenging task, particularly in complex geometries. In this work, this issue is handled with the lattice Boltzmann method (LBM), motivated by the similarities between the closure relations of the reflection-type boundary schemes equipping the LBM equation and the slip velocity condition established by slip-flow theory. Based on this analogy, we derive, as central result, the structure of the LBM boundary closure relation that is consistent with the second-order slip velocity condition, applicable to planar walls. Subsequently, three tasks are performed. First, we clarify the limitations of existing slip velocity LBM schemes, based on discrete analogs of kinetic theory fluid-wall interaction models. Second, we present improved slip velocity LBM boundary schemes, constructed directly at discrete level, by extending the multireflection framework to the slip-flow regime. Here, two classes of slip velocity LBM boundary schemes are considered: (i) linear slip schemes, which are local but retain some calibration requirements and/or operation limitations, (ii) parabolic slip schemes, which use a two-point implementation but guarantee the consistent prescription of the intended slip velocity condition, at arbitrary plane wall discretizations, further dispensing any numerical calibration procedure. Third and final, we verify the improvements of our proposed slip velocity LBM boundary schemes against existing ones. The numerical tests evaluate the ability of the slip schemes to exactly accommodate the steady Poiseuille channel flow solution, over distinct wall slippage conditions, namely, no-slip, first-order slip, and second-order slip. The modeling of channel walls is discussed at both lattice-aligned and non-mesh-aligned configurations: the first case illustrates the numerical slip due to the incorrect modeling of slippage coefficients, whereas the second case adds the effect of spurious boundary layers created by the deficient accommodation of bulk solution. Finally, the slip-flow solutions predicted by LBM schemes are further evaluated for the Knudsen's paradox problem. As conclusion, this work establishes the parabolic accuracy of slip velocity schemes as the necessary condition for the consistent LBM modeling of the slip-flow regime.

DOI: 10.1103/PhysRevE.96.013311

I. INTRODUCTION

The classical hydrodynamic theory [1] is built on the assumption of a clear separation between two scales: one measuring the fluid intrinsic "molecularity," expressed by the mean-free path of molecules λ, and the other expressing the length scale of the flow process in study, determined by a characteristic geometrical length scale, such as the system size H. Their ratio defines the Knudsen number $\mathrm{Kn} = \lambda/H$. It is commonly accepted [2–5] that the continuum-flow assumption holds up to $\mathrm{Kn} \approx 0.001$. For $\mathrm{Kn} \leqslant 0.001$ the Navier-Stokes equations together with the no-slip boundary condition provide an accurate physical framework to describe fluid flows. However, with the increase of Kn the continuum-flow regime breaks down and the first nonequilibrium effect is manifested in the description of the fluid-wall interactions: the so-called *slip-flow regime* ($0.001 < \mathrm{Kn} < 0.1$). In this case, although the continuum Navier-Stokes framework remains valid in bulk, at the solid boundaries the no-slip velocity condition is replaced by a slip one. This theoretical perspective concedes the accommodation of hydrodynamic solutions on slip boundaries, without any boundary layer modification. This contrasts with the subsequent nonequilibrium stage: the transition-flow regime ($0.1 < \mathrm{Kn} < 10$). Here, the fluid-wall nonequilibrium effects are no longer localized at the solid boundaries, but extend over a non-negligible portion of the bulk domain. These regions are called Knudsen boundary layers and tend to distort the velocity profile in a non-negligible way, being relevant in the context of transition flows.

This work focuses on low-speed, isothermal flows at finite Kn numbers, pertaining to the slip-flow regime. Such flow characteristics are commonly found in microfluidic applications, as described in [6–10] and references therein. This class of flows follows a hydrodynamic description in bulk, governed by Stokes equations:

$$\vec{\nabla} \cdot \vec{u} = 0, \quad \vec{F} - \vec{\nabla} P + \nu \rho_0 \nabla^2 \vec{u} = 0, \tag{1}$$

with $\vec{u}$ the fluid velocity, P the pressure, and $\vec{F}$ an external body force. A single-component fluid system is considered, which is characterized by density ρ_0 and kinematic viscosity ν. At boundaries, the model that describes the fluid-wall interaction assumes the *second-order slip velocity boundary condition* [11,12], whose nondimensional formulation for planar walls reads as

$$u_{t|\mathrm{wall}} - U_w = -C_1 \mathrm{Kn}\, \partial_n u_t|_{\mathrm{wall}} - C_2 \mathrm{Kn}^2 \partial_n^2 u_t\big|_{\mathrm{wall}}. \tag{2}$$

Above, u_t denotes the tangential component of the fluid velocity, U_w is the wall velocity, the derivatives of the velocity

*goncalo.nuno.silva@gmail.com

are taken in the outward direction of the wall normal (denoted by subscript n), and C_1 and C_2 refer to slippage coefficients, determined through different approaches (see Table I and the comprehensive reviews [11,13,14]). The formulation of Eq. (2) is built upon the following three aspects. First, Eq. (2) has a self-consistent structure, which is evident by the recovering of the no-slip condition $u_{t|\text{wall}} = U_w$ at the formal limit $\text{Kn} \to 0$ [whereas the first-order slip-flow model [15] is also restored as the first-order Kn expansion in Eq. (2)]. Second, the form of Eq. (2) only considers flows with constant slip velocity, i.e., where no variations occur along the wall surface, only gradients along the normal direction exist. Third, the application of Eq. (2) is limited to planar surfaces. For curved walls the consistent formulation of the slip velocity condition must consider additional terms, related to the surface curvature [3,11,14,16–18]. This case will be addressed in a future publication.

Compared to the first-order theory, originally formulated by Maxwell [15] (and independently by Navier [25] following a different reasoning), the inclusion of a second-order term (related with the flow curvature) in the slip velocity condition constitutes a significant improvement in the description of moderately rarefied gas flows. Indeed, this framework appears to provide, at least in the average sense, robust predictions in a variety of flow problems of practical interest, well beyond $\text{Kn} \approx 0.1$, the theoretically expected slip-flow validity limit [12,14]. For example, the Knudsen's paradox [2,12,13], i.e., the nonmonotonic Kn dependence of the mass flux in steady Poiseuille flow, featuring a minimum well within the transition regime, can be captured in the frame of the second-order slip-flow theory. Its applicability may even extend up to $\text{Kn} \approx 2$ with more elaborate second-order slip models, e.g., [20]. We refer to [3,4,11–14], for more details on the strengths and limitations of the slip-flow theory. Here, we assume that Eq. (2) is valid and the specific values of coefficients C_1 and C_2 are available, e.g., from Table I or from comprehensive databases as in [3,11,13], and they accurately describe the physics at hand. Taking for granted such hypotheses, our focus is dedicated to the specific challenges posed by the discretization of Eq. (2). Mathematically, the problem can be stated as the numerical implementation of a Robin-type boundary condition for the tangential velocity. The objective is that the discrete representation of such a slip velocity model, and in particular its coefficients, do not get modified by numerical errors, so that simulations are consistent with the physical slip condition imposed. This question is important since slip-flow theory offers incomparable advantages from the computational perspective. Given that it operates over continuum-based equations, this approach is substantially more economical than kinetic-based or molecular models, e.g., [26]. For that reason, various numerical methods to solve the Navier-Stokes equations with slip velocity boundary conditions have been developed. Examples are the finite volume method [27,28], finite difference method [29,30], or finite element method [31–33]. Still, the numerical approximation of the slip velocity condition in the frame of these traditional computational fluid dynamics (CFD) techniques is not a trivial task, particularly in complex geometries, e.g., [14,28,33,34]. Such a difficulty justifies the interest in alternative and competitive numerical formulations [34,35]. Here, we devote our attention to the lattice Boltzmann method (LBM).

The LBM [36–39] has been regarded, almost ever since its introduction, as a very promising approach to describe "beyond-hydrodynamics" phenomena [36,39,40]. As of today, the ability of the LBM equation to capture nonequilibrium phenomena at large Kn remains an active topic of research, e.g., [41–44] and references therein. Yet, so far, the more basic question on the performance of the LBM equation in the slip-flow regime has not been completely answered. At the moment, the vast majority of works addressing this topic, e.g., [45–56] (with the possible exception of [57]), have explored the relation between the LBM equation and the continuous Boltzmann-BGK equation [40,58,59]. In the derivation of LBM boundary schemes, such studies have considered either LBM discrete analogs of the Maxwell-Boltzmann [44,60,61] or other related kinetic-based boundary models [45,47,62]. Unfortunately, these LBM versions of kinetic boundary schemes are affected by critical limitations, most notably, by introducing a purely numerical slip that interferes with

TABLE I. Examples of C_1 and C_2 slippage coefficients determined through different approaches; a more complete list can be found in [14]. The parameter σ_v is the tangential momentum accommodation coefficient (TMAC). For most surfaces $\sigma_v \in [0.6,1]$ [14], where $\sigma_v = 1$ corresponds to fully diffusive walls. In this work, we take $\sigma_v = 1$, but other σ_v values have no impact on conclusions. Note the last two models present Kn-dependent coefficients. Wu (2008) [19] model depends on f_W, defined as $f_W = \min[\frac{1}{\text{Kn}},1]$. Wang *et al.* (2017) [20] model has been computed in this work through Eq. (11) with (B1) and (B2) of [20], the Ei denotes the exponential integral function defined as $\text{Ei}(x) = -\int_{-x}^{+\infty} t^{-1}\exp(-t)dt$.

References	C_1	C_2	Approach
Maxwell (1987) [15]	$\frac{2-\sigma_v}{\sigma_v}$	0	Elementary kinetic theory
Cercignani (1990) [21]	$1.1466\frac{2-\sigma_v}{\sigma_v}$	0.9756	Linearized Boltzmann-BGK
Hadjiconstantinou (2003) [22]	$1.11\frac{2-\sigma_v}{\sigma_v}$	0.61	Hard sphere model
Lockerby *et al.* (2004) [23]	$\frac{2-\sigma_v}{\sigma_v}$	0.145–0.19	Maxwell-Burnett model
Struchtrup and Torrilhon (2008) [24]	$\frac{2-\sigma_v}{\sigma_v}$	0.531	R13-based model
Wu (2008) [19]	$\frac{2}{3}\left[\frac{3-\sigma_v f_W^3}{\sigma_v} - \frac{3(1-f_W^2)}{2\text{Kn}}\right]$	$\frac{2}{3}\left[f_W^4 + \frac{2}{\text{Kn}^2}(1-f_W^2)\right]$	Advanced kinetic theory
Wang *et al.* (2017) [20]	$\frac{2\sigma_v\text{Kn}(\text{Kn}^2+\text{Kn}-1) - 2\exp\left(\frac{1}{\text{Kn}}\right)\left[\text{Kn}^3(\sigma_v-2)+\sigma_v\text{Ei}\left(-\frac{1}{\text{Kn}}\right)\right]}{3\sigma_v\text{Kn}\left\{\frac{(\text{Kn}-1)\text{Kn}}{+\exp\left(\frac{1}{\text{Kn}}\right)\left[\text{Kn}^2+\text{Ei}\left(-\frac{1}{\text{Kn}}\right)\right]}\right\}}$	$\frac{\text{Kn}[-1+\text{Kn}(1+\text{Kn})] - \exp\left(\frac{1}{\text{Kn}}\right)\left[2\text{Kn}^4+\text{Ei}\left(-\frac{1}{\text{Kn}}\right)\right]}{4\text{Kn}^2\left\{\frac{(\text{Kn}-1)\text{Kn}}{+\exp\left(\frac{1}{\text{Kn}}\right)\left[\text{Kn}^2+\text{Ei}\left(-\frac{1}{\text{Kn}}\right)\right]}\right\}}$	Advanced kinetic theory

the physical slip condition. While the elimination of this artifact was attempted in the past [49–51,54], specifically, for the case of a (force-driven) Poiseuille flow in the slip-flow regime, by calibrating the coefficient(s) in the kinetic LBM boundary schemes to "absorb" the discrete lattice effects into physical terms, still limitations subsist, even after calibration. The reason is intrinsic to their formulation. Similarly to the bounce-back (BB) rule as a no-slip model, these so-called "kinetic" LBM boundary schemes are based on low-order discretizations of the slip velocity condition. However, unlike in the hydrodynamic case, where improvements over the BB rule as no-slip boundary condition have been proposed, e.g., [63,64], a general and consistent solution to handle the slip condition has not been given yet, to the best of our knowledge.

The main objective of this work is, therefore, to improve the limitations previously identified and to place LBM as a consistent CFD tool for moderately rarefied gas flow problems (which may possibly be extended over larger Kn values with specific add ons as reviewed by [41]). Our starting point is the recognition that the reflection-type boundary rules equipping the LBM provide a rather natural groundwork to model the slip velocity boundary condition, as given by Eq. (2). The reason is that the prescription of both conditions shares a similar structure in terms of Taylor series closure relation. Hence, the LBM working principle can offer advantages over standard CFD methods in this class of problems. For instance, the LBM reflection-type boundary schemes can naturally handle the velocity derivatives at the boundary without the necessity of any explicit computations, e.g., through finite differences. This feature simplifies its application to complex geometries and may also improve the algorithm efficiency by reducing the span of grid nodes required.

The inherent difficulty with the development of LBM models is that conditions for the hydrodynamic variables (e.g., velocity, pressure, etc.) are determined by particle's dynamical rules, expressed at the mesoscopic level. Typically, the relation between these two levels of description is not evident, demanding the use of multiscale analyses, such as the Chapman-Enskog expansion [65,66]. Although, care should be taken as the Chapman-Enskog expansion does not permit describing the solution inside accommodation (Knudsen) layers [4]; in the LBM context this issue has been addressed through alternative theoretical perspectives [67–69], yet the study of such layers is not pursued herein. In this work, we use the Chapman-Enskog expansion to show that the consistent LBM modeling of the slip velocity condition (of either first or second order) is intrinsically tied in with the order of accuracy of the LBM boundary scheme, where the necessary condition amounts to the scheme *parabolic accuracy*. Otherwise, the LBM boundary scheme will unavoidably introduce numerical artifacts at the same order of the physical slip coefficients. This interference will disturb the effective slip velocity condition and in turn cause the numerical slip at the boundary, which is the defect we wish to avoid. As solution method, rather than persisting in deriving LBM analogs of kinetic-based boundary schemes, we propose a general LBM framework where the slip velocity condition is implemented through the multireflection procedure [63,64]. Aside from guaranteeing the consistency of the slip velocity model, the class of LBM boundary schemes constructed in this work also supports arbitrary plane wall discretizations on the LBM uniform mesh formulation, without any extra effort. The importance of the correct wall discretization is perceived on the accommodation of the bulk solution; whenever not sufficiently accurate it leads to the creation of spurious boundary layers, which may be confused with physical Knudsen layers. We will illustrate both theses issues, i.e., the numerical wall slip and the spurious boundary layers, for a Poiseuille flow in the slip-flow regime, with the channel discretized in lattice-aligned and lattice-inclined configurations.

The paper is organized as follows. Section II reviews the LBM structure, with focus on the two-relaxation-time (TRT) collision scheme. The first part addresses the evolution equation of the LBM-TRT, and the second part discusses its macroscopic limit. Section III derives the closure relation of the second-order slip velocity condition supported by linkwise LBM boundary schemes. Section IV critically discusses the capabilities and limitations of existing "kinetic" LBM boundary schemes. Section V proposes an alternative class of local schemes that implement the slip condition consistently, with the aid of specific calibration strategies. Section VI constructs a generic class of two-point boundary schemes, based on the multireflection framework, which consistently handle the slip velocity condition, supporting it at arbitrary wall and lattice distances and/or orientations. Section VII evaluates the performance of such slip velocity LBM boundary schemes taking as benchmark test the classical steady Poiseuille flow problem. Section VIII reports on complementary simulation results based on the Knudsen's paradox problem. Section IX concludes the study. At the end of the paper, two Appendices are included. Appendix A briefly revises other LBM collision operators with relevance to this study. Appendix B demonstrates the equivalence between the schemes developed in Sec. IV and the scheme proposed in [56].

II. LATTICE BOLTZMANN METHOD

A. Two-relaxation-time (TRT) scheme

The lattice Boltzmann method (LBM) [36,37,70–72] is used to solve Eq. (1). The LBM working principle is based on the tracking of populations $f_q(\vec{x},t)$, defined on space $\vec{x}$ and time t, along a discrete velocity set (also called lattice), which features one immobile $\vec{c}_0 = \vec{0}$ and $Q_m = Q - 1$ nonzero velocity vectors $\vec{c}_q$ per grid node. The first $Q_m/2$ velocity vectors $\vec{c}_q$ are set diametrically opposite to the other $Q_m/2$ vectors $\vec{c}_{\bar{q}} = -\vec{c}_q$, where the pair $\{\vec{c}_q, \vec{c}_{\bar{q}}\}$ is referred to as a link. Here, we employ the d-dimensional lattice with Q velocities given by $d = 2$ and $Q = 9$, called $d2Q9$ model [71]. The update of LBM evolves along a succession of streaming [Eq. (3a)] and collision [Eq. (3b)] steps. For the collision we adopt the TRT model [64] so that the LBM follows the evolution equation:

$$f_q(\vec{x}+\vec{c}_q,t+1) = \tilde{f}_q(\vec{x},t), \quad q = 0,1,\ldots,Q-1 \tag{3a}$$

$$\tilde{f}_q(\vec{x},t) = [f_q + g_q^+ + g_q^- + S_q^+ + S_q^-](\vec{x},t), \quad q = 0,1,\ldots,\frac{Q_m}{2}$$

$$\tilde{f}_{\bar{q}}(\vec{x},t) = [f_{\bar{q}} + g_q^+ - g_q^- + S_q^+ - S_q^-](\vec{x},t), \quad q = 1,\ldots,\frac{Q_m}{2}. \tag{3b}$$

The term $\tilde{f}_q$ denotes the post-collision state of populations f_q. Other terms in Eq. (3b) are $S_q^{\pm}$, which account for mass S_q^+ and momentum S_q^- sources, and $g_q^{\pm} = -s^{\pm}(f_q^{\pm} - e_q^{\pm})$, which express post-collision nonequilibrium quantities. These latter are given by (i) two values $f_q^{\pm} = \frac{f_q \pm f_{\bar{q}}}{2}$ for each discrete-velocity link $\{\vec{c}_q, \vec{c}_{\bar{q}}\}$; (ii) two equilibrium values $e_q^{\pm}$, which are detailed below [see Eq. (4)]; and (iii) two relaxation parameters $s^{\pm} \in]0,2[$ that define two eigenfunctions $\Lambda^{\pm} = (\frac{1}{s^{\pm}} - \frac{1}{2})$, whose product $\Lambda = \Lambda^+\Lambda^-$ controls nondimensional steady-state solutions [64,73]. In solving Eq. (1) the equilibrium functions $e_q^{\pm}$ take a linear form, with e_q^+ describing mass density ρ (or pressure P) and e_q^- designating momentum density $\vec{j} = \rho_0\vec{u}$, where $\vec{u}$ is the velocity and ρ_0 a constant density state [66,74]:

$$e_q^+ = P_q, \quad P_q = t_q P(\rho), \quad e_0 = \rho - 2\sum_{q=1}^{Q_m/2} e_q^+,$$

$$e_q^- = j_q, \quad j_q = t_q(\vec{j}\cdot\vec{c}_q) = t_q\rho_0(\vec{u}\cdot\vec{c}_q). \tag{4}$$

The relation $P(\rho)$ assumes the equation of state $P = c_s^2\rho$, with $c_s^2 \in]0,1]$ a free parameter, further restricted by velocity-set dependent stability conditions [75,76]. We adopt for t_q isotropic weights [71], e.g., $\{t_q^{(I)}, t_q^{(II)}\} = \{\frac{1}{3}, \frac{1}{12}\}$ in $d2Q9$. The source term is implemented according to previous works [77–79], and projected onto the TRT basis [64]. In this respect, we note the existence of other equivalent source term formulations [64]. In this study, we consider no mass source (nor symmetric force corrections [79]), and the momentum source prescribes the force density $\vec{F}$:

$$S_q^+ = 0, \quad S_q^- = s^-\Lambda^- F_q, \quad F_q = t_q(\vec{F}\cdot\vec{c}_q). \tag{5}$$

The macroscopic fluid quantities are computed through zeroth- and first-order moments of f_q^+ and f_q^-, respectively:

$$\rho = f_0 + 2\sum_{q=1}^{Q_m/2} f_q^+, \quad \vec{j} = \vec{J} + \frac{1}{2}\vec{F}, \quad \vec{J} = 2\sum_{q=1}^{Q_m/2} f_q^-\vec{c}_q,$$

$$\vec{F} = 2\sum_{q=1}^{Q_m/2} F_q\vec{c}_q. \tag{6}$$

To conclude, we note that although the TRT framework will be primarily utilized in this work, our results apply to other collision models. Such a generality is relevant since a multitude of LBM collision operators have been adopted to simulate gaseous flows in the slip-flow regime. A far from exhaustive list of references includes for the multiple relaxation time (MRT) [50,51,55,56,62,80], for the regularized (REG) [80–87], and for the single relaxation time [Bhatnagar-Gross-Krook (BGK)] [47–49,52,60,61,88–91]. In Appendix A we briefly revise the working principle of these three collision operators, together with their relation to TRT. Also in Appendix A we introduce a new version of the REG operator, labeled "symmetrized" REG (S-REG), which corresponds to a subclass of the TRT scheme where the antisymmetric modes (controlled by Λ^-) are filtered out during collision. This is in the spirit of the filtering out of higher-order modes by original REG [81,82,92]. The REG and S-REG operators share numerous similarities, which are pointed out in Appendix A. For the purpose of the ensuing analysis, we summarize in Table II the relaxation parameters supported by the three collision operators that will be considered herein, namely, TRT, REG/S-REG, and BGK. The MRT and the extra degrees of collision are not explored in this work. The reason is that, in this class of problems and for the purpose of accuracy, only two relaxation modes appear to be relevant and those are the TRT modes; such a result has been extensively reported in literature, e.g., [50,51,55,56,62,80], and also confirmed by our numerical tests (more details in Appendix A).

TABLE II. Relation between the relaxation parameters supported by the collision schemes used in this study: the generic TRT and its subclasses S-REG and BGK. The relation between TRT and MRT is discussed in Appendix A.

	TRT	REG/S-REG	BGK
Λ^+	3ν	3ν	3ν
Λ^-	$\forall\, \mathbb{R}^+$	$\frac{1}{2}$	3ν
Λ	$\forall\, \mathbb{R}^+$	$\frac{3}{2}\nu$	$9\nu^2$

B. Macroscopic limit

The macroscopic limit of the LBM equations can be determined through the second-order Chapman-Enskog analysis [65,66]. By "second order" we mean the truncation of the expansion at $\mathcal{O}(\epsilon^3)$, where ϵ is the smallness parameter of perturbation, taken as the ratio of the lattice unit and the characteristic length scale H (expressed in simulation units), i.e., $\epsilon = 1/H$. We note that ϵ and the Knudsen number Kn have different meanings. While ϵ is a grid scale parameter, Kn is a nondimensional group that controls the physical regime. Hence, with Kn fixed, the terms of higher order in ϵ should be interpreted as truncation errors and the limit $\epsilon \to 0$ as the zero mesh spacing.

For the perturbation analysis we employ the steady-state Chapman-Enskog ansatz of [93], which provides a systematic procedure to derive the full (infinite) solution of the series. On this basis, the second-order expansion unfolds the steady-state structure of the nonequilibrium post-collision quantities $g_q^{\pm}$ as follows:

$$g_q^{\pm} = \partial_q(e_q^{\mp} - \Lambda^{\mp}\partial_q e_q^{\pm}) - S_q^{\pm} + \mathcal{O}(\epsilon^3), \tag{7}$$

where, after introducing Eqs. (4) and (5) into Eq. (7), each individual component reads as

$$g_q^+ = \partial_q j_q,$$

$$g_q^- = \partial_q P_q - \Lambda^+\partial_q^2 j_q - s^-\Lambda^- F_q, \tag{8}$$

with $\partial_q^k = (\vec{c}_q\cdot\vec{\nabla})^k$ for $k \geqslant 1$. In deriving Eq. (8) we assumed (i) $\partial_q^2 P_q = 0$, due to the Stokes flow condition, and (ii) $\vec{F} = \text{const}$. Next, we invoke the exact mass and momentum conservation principles, respectively,

$$\sum_{q=0}^{Q-1} g_q^+ = 0, \quad 2\sum_{q=1}^{Q_m/2} \vec{c}_q g_q^- = \frac{s^-\vec{F}}{2}. \tag{9}$$

Finally, we introduce Eq. (8) into Eq. (9) and compute the velocity moments based on Eq. (6), with the help of lattice constraints $2\sum_{q=1}^{Q_m/2} t_q c_{q\alpha} c_{q\beta} = \delta_{\alpha\beta}$ and $6\sum_{q=1}^{Q_m/2} t_q c_{q\alpha}^2 c_{q\beta}^2 = 1 + 2\delta_{\alpha\beta}$, where $\delta_{\alpha\beta}$ is the Kronecker delta. The outcome provides the steady incompressible Stokes equations (1), with kinematic viscosity $\nu = \frac{\Lambda^+}{3}$. We remark that, up to this second order, the recovered LBM macroscopic equations only depend on Λ^+. Therefore, from Table II one infers that the different LBM collision models coincide within this level of approximation. However, at higher orders, the structure of the relaxation parameters, which appear as coefficients in the spatial (truncation) corrections, depend on Λ (cf. [73,76,93,94]). Thus, looking again at Table II, it is concluded that the discrete macroscopic equations satisfied by those LBM collision models are fundamentally different. While the spatial truncation errors in BGK scale with $\Lambda = 9\nu^2$, in REG they scale with $\Lambda = \frac{3}{2}\nu$ whereas in TRT (and also MRT) they are ν independent. These results are qualitatively discussed in Appendix A. For a more rigorous discussion on the role of Λ and the potential ν dependence of numerical errors we refer to [73,76,93,94].

III. LATTICE BOLTZMANN CLOSURE RELATION OF SECOND-ORDER SLIP VELOCITY MODEL

This section focuses on the closure relation of generic linkwise LBM boundary schemes viewing the consistent modeling of the slip-flow regime. Derivations are performed for the second-order slip velocity model, where the first-order slip and the no-slip conditions appear as particular cases.

A. Generic formulation of second-order slip velocity

Since we are interested in formulating the slip velocity condition at arbitrarily oriented wall-lattice positions, the subsequent analysis is performed on the two-dimensional (2D) rotated Cartesian coordinate system $\vec{x}\,' = \{x', y'\}$. This reference frame $\vec{x}\,'$ may rotate an angle θ with respect to the 2D lattice-aligned fixed reference frame, denoted as $\vec{x} = \{x, y\}$. The two frames relate as $x' = x\cos\theta + y\sin\theta$ and $y' = -x\sin\theta + y\cos\theta$, whereby the axes x' and y' align with the tangent and the normal wall vectors, respectively. Based on this convention, the wall normal unit vector $\vec{n}'$ is defined to point *outward* the fluid domain, i.e., $\vec{n}' = -\vec{1}_{y'}$ on a bottom wall and $\vec{n}' = \vec{1}_{y'}$ on a top wall; the wall tangential unit vector $\vec{t}'$ is defined as $\vec{t}' = \vec{1}_{x'}$. Figure 1 illustrates the wall-lattice system in aligned and inclined configurations. The fluid velocity vector is $\vec{u}\,' = \{u_{x'}, u_{y'}\}$. Although the subsequent analysis is illustrated for a 2D case, the derivations presented below apply similarly to three-dimensional (3D) domains.

Consider a *plane wall* and let $\vec{x}_w{}'$ be a boundary point with local gradient $\vec{\nabla}' = \{\partial_{x'}, \partial_{y'}\}$. Let the wall be rigid (i.e., undeformable) and impermeable: $\vec{u}\,'(\vec{x}_w{}') \cdot \vec{n}' = u_{y'}(\vec{x}_w{}') = 0$, and the tangential component of the fluid velocity at the wall $\vec{u}\,'(\vec{x}_w{}') \cdot \vec{t}' = u_{x'}(\vec{x}_w{}')$ differ from the wall tangential velocity $\vec{U}_w{}' \cdot \vec{t}' = U_w{}'$ (where $U_w{}' = 0$ for a resting wall) by an amount proportional to (the normal component of) the first- and second-order velocity gradients at the wall. This jump condition corresponds to the second-order slip velocity boundary model [13,14,35,95,96]:

$$[\vec{u}\,'(\vec{x}_w{}') - \vec{U}_w{}'] \cdot \vec{t}' = -C_1\lambda\, \vec{n}' \cdot \vec{\nabla}'\vec{u}\,'|_{\vec{x}_w{}'} \cdot \vec{t}' - C_2\lambda^2\, \vec{n}'\vec{n}' : \vec{\nabla}'\vec{\nabla}'\vec{u}\,'|_{\vec{x}_w{}'} \cdot \vec{t}'. \quad (10)$$

We note that Eq. (10) is the dimensional form of Eq. (2), previously given in Sec. I. The two formulations are related by $\mathrm{Kn} = \lambda/H$, where λ and H refer to microscopic and macroscopic reference length scales, respectively.

B. Linkwise formulation of second-order slip velocity

According to Eq. (10) the structure of the slip velocity condition is described by the Taylor series of the fluid velocity at the wall. Interestingly, a similar Taylor-type structure is found in the closure relation of the reflection-type boundary schemes used by LBM [63,64,67,94,97]. The difference lies in the meaning of these expansions. While the slip velocity condition (10) applies at the wall position $\vec{x}_w{}'$ with the coefficients quantifying the degree of wall slippage, the linkwise LBM boundary schemes [e.g., Eq. (20) for the bounce back or Eq. (14) for the multireflection schemes] obey a closure relation which applies at the boundary node position $\vec{x}_b{}'$ with the coefficients quantifying its distance to the wall site $\vec{x}_w{}'$. Therefore, the formulation of the slip velocity condition in the LBM framework requires (i) to reexpress Eq. (10) at boundary node $\vec{x}_b{}'$ and (ii) to modify the coefficients accordingly.

In order to transform Eq. (10) from $\vec{x}_w{}'$ to $\vec{x}_b{}'$, let us introduce the wall cut-link distance δ_q defined by $\vec{x}_w{}' = \vec{x}_b{}' + \delta_q\, \vec{c}_q{}'$ (see Fig. 1), where $\vec{c}_q{}' = \{c_{qx'}, c_{qy'}\}$ denotes the particle velocity also expressed in the rotated frame. According to the Chapman-Enskog analysis, the spatial derivative operator scales as $\mathcal{O}(\epsilon)$, and since our analysis excludes terms of $\mathcal{O}(\epsilon^3)$, we expand each term in Eq. (10) up to the second differential order:

$$\begin{aligned}
\vec{u}\,'(\vec{x}_w{}') &= \vec{u}\,'(\vec{x}_b{}' + \delta_q\, \vec{c}_q{}') \simeq \vec{u}\,'(\vec{x}_b{}') + \delta_q\, \vec{c}_q{}' \cdot \vec{\nabla}'\vec{u}\,'|_{\vec{x}_b{}'} \\
&\quad + \frac{\delta_q^2}{2}\, \vec{c}_q{}'\vec{c}_q{}' : \vec{\nabla}'\vec{\nabla}'\vec{u}\,'|_{\vec{x}_b{}'} + \mathcal{O}(\epsilon^3), \\
\vec{\nabla}'\vec{u}\,'(\vec{x}_w{}') &= \vec{\nabla}'\vec{u}\,'(\vec{x}_b{}' + \delta_q\, \vec{c}_q{}') \simeq \vec{\nabla}'\vec{u}\,'|_{\vec{x}_b{}'} \\
&\quad + \delta_q\, \vec{c}_q{}' \cdot \vec{\nabla}'\,\vec{\nabla}'\vec{u}\,'|_{\vec{x}_b{}'} + \mathcal{O}(\epsilon^3), \\
\vec{\nabla}'\vec{\nabla}'\vec{u}\,'(\vec{x}_w{}') &= \vec{\nabla}'\vec{\nabla}'\vec{u}\,'(\vec{x}_b{}' + \delta_q\, \vec{c}_q{}') \simeq \vec{\nabla}'\vec{\nabla}'\vec{u}\,'|_{\vec{x}_b{}'} + \mathcal{O}(\epsilon^3).
\end{aligned} \quad (11)$$

The expansions in Eq. (11) are introduced into Eq. (10), and the terms of identical differential order are grouped as follows:

$$\vec{u}\,'(\vec{x}_b{}') + (\delta_q\, \vec{c}_q{}' + C_1\lambda\, \vec{n}') \cdot \vec{\nabla}'\vec{u}\,'|_{\vec{x}_b{}'} + \left(\frac{\delta_q^2}{2}\vec{c}_q{}'\vec{c}_q{}' + C_1\lambda\,\delta_q\, \vec{c}_q{}'\vec{n}' + C_2\lambda^2\, \vec{n}'\vec{n}'\right) : \vec{\nabla}'\vec{\nabla}'\vec{u}\,'|_{\vec{x}_b{}'} = \vec{U}_w{}'. \quad (12)$$

Above, the dependence on $\vec{t}'$ has been dropped taking into account that $\vec{u}\,'(\vec{x}_w{}')$ and $\vec{t}'$ are parallel vectors since $\vec{u}\,'(\vec{x}_w{}') \cdot \vec{n}' = 0$ due to the wall impermeability condition. As a last step, we project Eq. (12) onto $\vec{c}_q{}'$. To denote the lattice space projection, the following notation is introduced: $\partial_q^k = (\vec{c}_q{}' \cdot \vec{\nabla}')^k$ for $k \geqslant 1$, and $\Theta_q = (\vec{c}_q{}' \cdot \vec{n}')$. The parameter

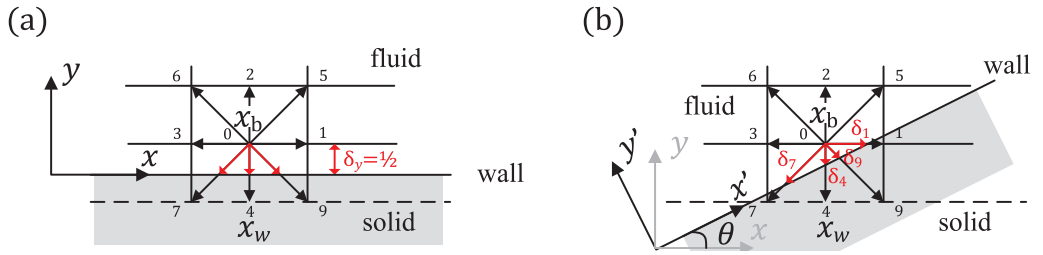

FIG. 1. Discretization of wall on LBM uniform mesh: (a) lattice-aligned wall and (b) lattice-inclined wall.

Θ_q represents the projection of the outgoing particle velocity $\vec{c}_q{}'$ on the outward unit normal vector to the wall $\vec{n}'$ (note, $\Theta_q > 0$ because both vectors point outward). Then, the result is remapped onto the Cartesian fixed frame $\vec{x}$ by the coordinate transformation, e.g., $j_q = t_q \rho_0 (\vec{u}\,' \cdot \vec{c}_q{}') = t_q \rho_0 (\vec{u} \cdot \vec{c}_q)$. In the end, we obtain the LBM closure relation for the second-order slip velocity model, expressed by Eq. (13), and valid at an arbitrary wall cut-link distance $\delta_q = (\vec{x}_w - \vec{x}_b)/\vec{c}_q$:

$$
\begin{aligned}
& j_q(\vec{x}_b) + \alpha_q^+ \partial_q j_q(\vec{x}_b) + \alpha_q^- \partial_q^2 j_q(\vec{x}_b) = j_{q\,w}(\vec{x}_w), \\
& \alpha_q^+ = (\delta_q + C_1 \lambda_q), \quad \alpha_q^- = \left(\frac{\delta_q^2}{2} + C_1 \lambda_q \delta_q + C_2 \lambda_q^2 \right), \\
& \lambda_q = \frac{\lambda}{\Theta_q}.
\end{aligned}
\tag{13}
$$

We note that in deriving Eq. (13) the following identities have been used: $\vec{n}' \cdot \vec{\nabla}\,' \psi = (\frac{\vec{n}' \cdot \vec{n}'}{\vec{c}_q{}' \cdot \vec{n}'}) \partial_q \psi = \frac{1}{\Theta_q} \partial_q \psi$ and $\nabla'^2 \psi = (\frac{\vec{n}' \cdot \vec{n}'}{(\vec{c}_q{}' \cdot \vec{n}')^2}) \partial_q^2 \psi = \frac{1}{\Theta_q^2} \partial_q^2 \psi$, where ψ denotes an arbitrary quantity.

C. Self-consistency of Eq. (13) with respect to other (lower-order) velocity boundary conditions

The self-consistent structure of the linkwise slip velocity closure relation, given by Eq. (13), can be recognized with respect to the following two limits. The first limit occurs when the wall coincides with the boundary node location $\vec{x}_b = \vec{x}_w$, i.e., $\delta_q = 0$ in Eq. (13). This case recovers the original slip velocity condition (10) projected onto particle velocity space $\vec{c}_q$. The second limit is identified when the continuum-flow regime is met, i.e., setting $\lambda = 0$ (with H finite, so that Kn $= 0$). This corresponds to the zeroth-order (no-slip) limit. When applied to Eq. (13), it leads to the familiar linkwise closure relation for the *no-slip condition* employed in numerous past studies, e.g., [63,64,67,94,97]:

$$
\begin{aligned}
& j_q(\vec{x}_b) + \alpha_q^+ \partial_q j_q(\vec{x}_b) + \alpha_q^- \partial_q^2 j_q(\vec{x}_b) = j_{q\,w}(\vec{x}_w), \\
& \alpha_q^+ = \delta_q, \quad \alpha_q^- = \frac{\delta_q^2}{2}.
\end{aligned}
\tag{14}
$$

The first-order limit recovered from Eq. (13) reveals that, while the "physical" *first-order slip velocity condition* only involves first-order derivatives of the velocity solution [e.g., see Eq. (10) with $C_1 \neq 0$ and $C_2 = 0$], its transcription into the LBM frame requires accounting for the coefficient of the Laplacian term as well. This result comes clear by setting $C_2 = 0$ in Eq. (13), which leads to

$$
\begin{aligned}
& j_q(\vec{x}_b) + \alpha_q^+ \partial_q j_q(\vec{x}_b) + \alpha_q^- \partial_q^2 j_q(\vec{x}_b) = j_{q\,w}(\vec{x}_w), \\
& \alpha_q^+ = (\delta_q + C_1 \lambda_q), \quad \alpha_q^- = \left(\frac{\delta_q^2}{2} + C_1 \lambda_q \delta_q \right), \\
& \lambda_q = \frac{\lambda}{\Theta_q}.
\end{aligned}
\tag{15}
$$

Looking at the zeroth-, first-, and second-order slip closure relations, respectively given by Eqs. (14), (15), and (13), it is worthwhile to discuss the role of the second-order term, related to the velocity Laplacian, as this term is often overlooked in traditional LBM boundary schemes, e.g., [98–100]. For the zeroth-order (no-slip) condition (14), the nonconsideration of the Laplacian term, i.e., the sole prescription of $j_q + \delta_q \partial_q j_q|_{\vec{x}_b} = j_{q\,w}(\vec{x}_w)$, renders the scheme second-order accurate since $\frac{\delta_q^2}{2} \partial_q^2 j_q \sim \mathcal{O}(\epsilon^2)$. This is the accuracy of most no-slip schemes in LBM, e.g., [98–100]. However, this accuracy degrades when the "slip order" increases. Already for the first-order slip condition the importance of the Laplacian term comes clear. Given that λ scales with H (with Kn fixed), i.e., $\lambda = \text{Kn}/\epsilon \sim \mathcal{O}(\epsilon^{-1})$, the neglect of the C_1 dependence at α_q^- will render the accuracy of the slip boundary scheme formally first order due to the order of magnitude of the term $C_1 \lambda_q \delta_q \partial_q^2 j_q \sim \mathcal{O}(\epsilon)$. Evidently, in the modeling of the C_2 coefficient the importance of the velocity Laplacian term becomes even more critical. Since $\lambda^2 = \text{Kn}^2/\epsilon^2 \sim \mathcal{O}(\epsilon^{-2})$, it follows that $C_2 \lambda_q^2 \partial_q^2 j_q \sim \mathcal{O}(1)$. This implies that any LBM slip boundary scheme which is not designed to be parabolic exact, as the multireflection schemes [63,64,94], becomes formally zeroth-order accurate with respect to the second-order slip condition. These conclusions will be confirmed by numerical tests in Sec. VII.

IV. ANALYSIS OF EXISTING "KINETIC" SLIP VELOCITY BOUNDARY SCHEMES

Based on the LBM closure relation given by Eq. (13), this section analyzes some of most commonly used fluid-wall interaction schemes to model the slip velocity boundary condition in LBM. For the analysis purpose, we focus on the *lattice-aligned channel* configuration, with walls parallel to either horizontal or diagonal links. These geometries are depicted in Figs. 2(a) and 2(b), respectively. Our derivations are performed on the rotated coordinate frame $\vec{x}' = \{x', y'\}$. In this frame, the flow is unidirectional $\vec{u} = \{u_{x'}, 0\}$ and respects the

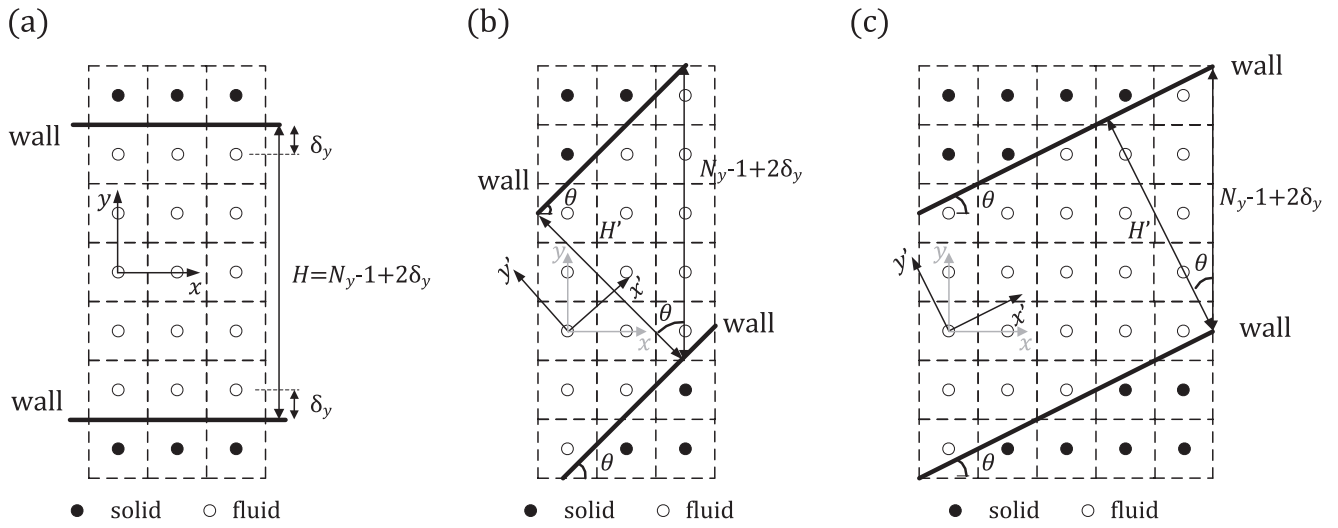

FIG. 2. Different flow-lattice configurations. (a) Discretization of horizontal channel ($\theta = 0$) with effective channel width given by $H = N_y - 1 + 2\delta_y$, where N_y is number of computational cells and δ_y is wall to grid node vertical distance. (b) Discretization of diagonal channel ($\theta = \pi/4$). (c) Discretization of arbitrarily inclined channel [$\theta = \tan^{-1}(\frac{1}{2})$]. The effective channel width is determined as $H' = H\cos\theta$, where H stands for the lattice-aligned case.

following conditions: (i) time independency $\partial_t u_{x'} = 0$, and (ii) streamwise invariance $\partial_{x'} u_{x'} = 0$. The flow is driven by either a constant body force $F_{x'}$, a constant pressure gradient $-\partial_{x'} P$, or by both. The channel walls are located at $\vec{x}_w{}'$ and move with velocity $\vec{U}_w{}'$ ($\vec{U}_w{}' = \vec{0}$ for a resting wall). Note that the rotating frame choice aims at identifying possible anisotropy effects, for which we consider the two cases (i) $\theta = 0$, where the channel aligns with the lattice horizontal links [Fig. 2(a)] and (ii) $\theta = \pi/4$, where the channel aligns with the lattice diagonal links [Fig. 2(b)]. The first case implies $\Theta_q^2 = \Theta^2 = 1$, whereas the second one yields $\Theta_q^2 = \Theta^2 = \frac{1}{2}$. In the same way, λ_q is represented as $\lambda_\Theta = \lambda/\Theta$, which implies that $\lambda_\Theta = \lambda$ in horizontal or $\lambda_\Theta = \sqrt{2}\lambda$ in diagonal channel. Likewise, for lattice-aligned channels, the distance from the wall to the boundary node is constant, which means δ_q reduces to $\delta_{y'}$. The derivations presented below apply over the nontrivial wall cut links $c_{qx'} c_{qy'} \neq 0$ (since the other wall cut link $c_{qy'}^2$ satisfies the trivial hydrostatic balance condition, e.g., [37]).

The analysis developed in this section focuses on the LBM slip schemes formulated as a combination of previously existing elementary reflection rules, such as bounce back [80,82,87–91,101,102], specular reflection [45,47,103–105], and diffusive Maxwell's reflection kinetic model [51,60,61,106]. To this group of schemes we call *combination "kinetic" (CK) schemes*. Here, the following CK schemes are analyzed: the combined bounce-back–specular-reflection (CBBSR) [45,47–51], the discrete Maxwell's diffuse-reflection (DMDR) [46,49,50,52,53], and the diffuse bounce-back (DBB) [51,54,55].

While the CK schemes were originally designed to operate at halfway walls, i.e., $\delta_{y'} = \frac{1}{2}$, in this section we generalize them to support arbitrary wall locations, i.e., $\delta_{y'} \in [0,1]$ (though limited to lattice-aligned configurations as discussed at the end of the section). This task has only been attempted in [56] for the DBB rule, and this scheme is shown to be equivalent to our general framework in Appendix B. With that in mind, this section has the following threefold objective: (i) to show how the theoretical framework developed here, to satisfy Eq. (13), easily allows to determine the calibration parameters of each CK scheme; (ii) to extend the general family of CK schemes from $\delta_{y'} = \frac{1}{2}$ to $\delta_{y'} \in [0,1]$; and (iii) to provide a critical analysis on the operation and limitation of the CK schemes.

Given that CBBSR, DMDR, and DBB schemes share an equivalent structure [49–51], they will be analyzed within a unified framework. This is represented through the common update rule given by Eq. (16), with coefficients $\{\mathcal{A}, \mathcal{B}, \mathcal{C}, \mathcal{D}\}$ summarized in Table III, which differentiate each case:

$$f_{\bar{q}}(\vec{x}_b, t+1) = \mathcal{A}\tilde{f}_q(\vec{x}_b, t) + \mathcal{B}\tilde{f}_j(\vec{x}_b, t) + \mathcal{C} f_{\bar{q}}^D(\vec{x}_b, t) + \mathcal{D} j_{\bar{q}\,w}(\vec{x}_w, t). \quad (16)$$

The first three terms on the right-hand side of Eq. (16) refer to the following elementary rules. First, $\tilde{f}_q$ comes from bounce back, where $\vec{c}_{\bar{q}} = -\vec{c}_q$. Second, $\tilde{f}_j$ comes from local specular reflection, where $c_{\bar{q}n} = -c_{jn}$ and $c_{\bar{q}t} = c_{jt}$ with the indices n and t denoting the normal and tangential components of the vector. Third, $f_{\bar{q}}^D = \mathcal{K} e_{\bar{q}}(\vec{x}_w)$ comes from diffusive Maxwell's reflection kinetic model, where $\mathcal{K} = \frac{\sum_{(\vec{c}_k{}' - \vec{U}_w{}')\cdot\vec{n}' > 0} |(\vec{c}_k{}' - \vec{U}_w{}')\cdot\vec{n}'| f_k}{\sum_{(\vec{c}_k{}' - \vec{U}_w{}')\cdot\vec{n}' < 0} |(\vec{c}_k{}' - \vec{U}_w{}')\cdot\vec{n}'| e_k} = 1$ for a lattice-aligned plane wall; the proof of this result can be found in the Appendix of [107] or in Sec. IV D of [61].

The derivation of the steady-state closure relation satisfied by Eq. (16) takes the following steps. First, we employ the decompositions $f_{\bar{q}} = e_q^+ - e_q^- - \frac{g_q^+}{s^+} + \frac{g_q^-}{s^-}$ and $\tilde{f}_q = e_q^+ + e_q^- + (1 - \frac{1}{s^+})g_q^+ + (1 - \frac{1}{s^-})g_q^- + S_q^-$ (and an equivalent expansion procedure to $\tilde{f}_j$). Second, we substitute them into Eq. (16), which leads to $(1 - \mathcal{A} - \mathcal{C}\mathcal{K})e_q^+ - (1 + \mathcal{A} - \mathcal{C}\mathcal{K})e_q^- - (\frac{1}{s^+} + \mathcal{A}(1 - \frac{1}{s^+}))g_q^+ + (\frac{1}{s^-} + \mathcal{A}(1 - \frac{1}{s^-}))g_q^- - \mathcal{A}S_q^- - \mathcal{B}(e_j^+ + e_j^- + (1 - \frac{1}{s^+})g_j^+ + (1 - \frac{1}{s^-})g_j^- + S_j^-) - \mathcal{D} j_{q\,w} = 0$. Third, we turn explicit the content of $e_q^\pm$, S_q^-, and $g_q^\pm$, by invoking the second-order Chapman-Enskog results

TABLE III. Coefficients of the boundary schemes for the generic update rule, given by Eq. (16), considering CBBSR [45–51], DMRD [49,50,52,53], DBB [51,54–56]. The r calibration is a function of C_1, ν, $\lambda_\Theta = \lambda/\Theta$, and possibly $\delta_{y'}$.

	CBBSR	DMDR	DBB
$\mathcal{A}$	r	0	r
$\mathcal{B}$	$(1-r)$	$(1-r)$	0
$\mathcal{C}$	0	r	$(1-r)$
$\mathcal{D}$	$2r$	0	$2r$
$r\vert_{\delta_{y'}=\frac{1}{2}}$ [Eq. (18)]	$\frac{3\nu}{3\nu+C_1\lambda_\Theta}$	$\frac{6\nu}{3\nu+C_1\lambda_\Theta}$	$\frac{3\nu-C_1\lambda_\Theta}{3\nu+C_1\lambda_\Theta}$
$r\vert_{\forall\,\delta_{y'}\in[0,1]}$ [Eq. (19)]	$\frac{3\nu}{(3\nu+C_1\lambda_\Theta)+(\delta_{y'}-1/2)}$	$\frac{6\nu}{(3\nu+C_1\lambda_\Theta)+(\delta_{y'}-1/2)}$	$\frac{(3\nu-C_1\lambda_\Theta)-(\delta_{y'}-1/2)}{(3\nu+C_1\lambda_\Theta)+(\delta_{y'}-1/2)}$

presented in Sec. II B. As the fourth and final step, we make use of the fact that these boundary schemes accommodate the bulk equation $\partial_{x'}P - F_{x'} = \frac{\Lambda^+}{3\Theta^2}\rho_0\partial^2_{y'}u_{x'}$. In the end, after some algebra, it can be shown that the general update rule of the CK schemes, given by Eq. (16), establishes at $\vec{x}_b$ for the wall cut links $c_{qx'}c_{qy'} \neq 0$, the slip velocity condition satisfying the steady-state closure relation

$$u_{x'} \mp \alpha^+\partial_{y'}u_{x'} + \alpha^-\partial^2_{y'}u_{x'} - \sigma\rho_0^{-1}\partial_{x'}P = \vec{U}'_w,$$
$$\alpha^+ = \left(\frac{1}{2} + 6\nu\sigma\right), \quad \alpha^- = \left(\frac{3\Theta^2-1}{3\Theta^2}\Lambda + 3\nu\sigma\right), \tag{17}$$

where the sign $\pm$ in α^+ depends on whether a bottom or top wall is considered. For each specific CK scheme we have $\sigma = \frac{1-r}{2r}$ in CBBSR [45–51], $\sigma = \frac{2-r}{2r}$ in DMDR [49,50,52,53], $\sigma = \frac{1-r}{2(1+r)}$ in DBB [51,54–56].

Now, we take a closer examination on the parameters featuring in Eq. (17). For now, let us assume that $\partial_{x'}P = 0$. In order to obtain the correct slip velocity condition, the coefficients $\alpha^\pm$ in Eq. (17) have to match those in Eq. (13). That is possible by finding proper values for the two calibration parameters: σ and Λ (or ν depending on the collision model adopted, see Table II). First, let us address the σ calibration, which will impact on the C_1 prescription. The σ parameter is determined by demanding a correct first-order coefficient, which is found by equating $\alpha^+ = (\frac{1}{2} + 6\nu\sigma)$ [Eq. (17)] to $\alpha^+ = (\delta_{y'} + C_1\lambda_\Theta)$ [Eq. (13)]. The simplest solution is recovered for a halfway wall, e.g. [49–53],

$$\sigma = \frac{C_1\lambda_\Theta}{6\nu} \quad \text{for } \delta_{y'} = \frac{1}{2}, \tag{18}$$

which otherwise generalizes to [56]

$$\sigma = \frac{(\delta_{y'} - 1/2) + C_1\lambda_\Theta}{6\nu} \quad \text{for } \delta_{y'} \in [0,1]. \tag{19}$$

With σ determined, the form of r follows immediately. The relations between σ and r are given in the paragraph below Eq. (17), whereby r parametrizes the coefficients appearing in Eq. (16). Table III summarizes the r calibrations for the three CK schemes. We highlight that the calibration of σ (or r) is collision model independent.

Second, let us address the Λ calibration, which further controls C_2. Upon establishing σ (to determine C_1), the Λ parameter is derived by demanding a correct second-order coefficient, found by equating $\alpha^- = (\frac{3\Theta^2-1}{3\Theta^2}\Lambda + 3\nu\sigma)$ [Eq. (17)] to $\alpha^- = (\frac{\delta^2_{y'}}{2} + C_1\lambda_\Theta\delta_{y'} + C_2\lambda^2_\Theta)$ [Eq. (13)]. Given that Λ is a collision-dependent parameter, its calibration will vary accordingly. Table IV summarizes the Λ solutions, for both halfway $\delta_{y'} = \frac{1}{2}$ and generic $\delta_{y'} \in [0,1]$ wall locations.

To conclude this section, we elaborate on specific defects inherent to CK schemes. The list of remarks enumerated below set the motivation to construct the improved LBM slip boundary schemes, presented in Secs. V and VI.

Remark 1. The usage of a viscosity and mean-free-path relationship, given by $\nu = \bar{\xi}\lambda$ where $\bar{\xi} \in \mathbb{R}^+$, is a very popular approach within this problem class, e.g., [41,49,50,54,88,105,108–111]. While the proportionality factor $\bar{\xi} = \frac{1}{3}\sqrt{\frac{6}{\pi}}$ was advocated as the "consistent choice" in [49,54,111], other values have been reported, e.g., [88,108,109]. In this regard, two notes are in order. First, in the slip-flow regime where ν is determined by hydrodynamics in bulk, any positive value of $\bar{\xi}$ is valid, providing its structure is consistently included in the boundary scheme calibration (this is not hard to infer from the direct substitution in Tables III and IV). Second, the advantage of adopting a relationship of the kind $\nu = \bar{\xi}\lambda$ is limited to $\delta_{y'} = \frac{1}{2}$. In this case, it permits removing the ν dependence from the calibration of σ. This is confirmed by inserting $\nu = \bar{\xi}\lambda$ into Eq. (18), which simplifies to $\sigma = \frac{C_1}{6\Theta\bar{\xi}}$. However, with viscosity-dependent collision operators, such as REG or BGK, a viscosity relationship of the kind $\nu(\lambda)$ is inconsistent since it will conflict with the viscosity $\Lambda(\nu)$ calibration on the α^- coefficient.

Remark 2. Although the presence of $\partial_{x'}P$ in Eq. (17) has been ignored in the above analysis, we note that these schemes are inconsistent for pressure-driven flows. One can confirm this defect in a simple Poiseuille flow developing in the slip-flow regime, and simultaneously driven by a body force and a pressure gradient. Consider a channel

TABLE IV. The Λ calibration for the generic update rule, given by Eq. (16), determined for different collision operators.We note that $\tilde{\alpha}^- = (\frac{3\Theta^2}{3\Theta^2-1})(\frac{1}{8} + C_2\lambda^2_\Theta)$ for $\delta_{y'} = \frac{1}{2}$ and $\tilde{\alpha}^- = (\frac{3\Theta^2}{3\Theta^2-1})(\frac{1}{2}(\delta^2_{y'} - \delta_{y'} + \frac{1}{2}) + C_1\lambda_\Theta(\delta_{y'} - \frac{1}{2}) + C_2\lambda^2_\Theta)$ for $\delta_{y'} \in [0,1]$.

	TRT	REG/S-REG	BGK
ν	$\forall\,\mathbb{R}^+$	$\frac{2}{3}\tilde{\alpha}^-$	$\frac{1}{9}\sqrt{\tilde{\alpha}^-}$
Λ	$\tilde{\alpha}^-$	$\frac{3}{2}\nu$	$9\nu^2$

with the following properties: width H, walls parallel to the horizontal lattice links $\Theta^2 = 1$, and cutting links halfway $\delta_y = \frac{1}{2}$. Further, assume the calibration of r and Λ to satisfy Tables III and IV, respectively. Even respecting these "ideal" conditions, the LBM solution rather than predicting $u_x^{(\text{exact})}(y) = \frac{(F_x - \partial_x P)}{8\rho_0 \nu}(H^2 - 4y^2 + 4C_1\lambda H + 8C_2\lambda^2)$ (details of this solution are given in Sec. VII A), it erroneously predicts $u_x(y) = u_x^{(\text{exact})}(y) + \frac{\partial_x P}{6\rho_0 \nu} C_1\lambda$, where this last term is the direct consequence of $\partial_{x'} P$ in Eq. (17) (details of this solution are given in Sec. VII B). As explained in Sec. VII, the removal of this pressure spurious term is possible in channel flows through a specific Λ calibration. However, its form differs depending on whether a force- or pressure-driven flow is simulated. Such a duality is clearly a drawback of CK schemes.

Remark 3. While we have extended the working principle of these CK schemes to support generic wall locations $\delta_{y'} \in [0,1]$, their applicability remains limited to lattice-aligned walls, contrary to what is implied in [56]. The cause for this limitation is the calibration of r and Λ, and that can be understood as follows. In order to handle arbitrary wall-lattice orientations, one has to consider the wall cut-link distance δ_q, a parameter that varies from link to link [cf. Fig. 1(b)]. However, the consideration of such a linkwise varying parameter δ_q (instead of the linkwise constant one $\delta_{y'}$) implies that, in the calibration of r and Λ, the tuning of the relaxation parameters needs to proceed in the same linkwise manner, i.e., in the spirit of the MRT-L model [73]. It follows that anisotropic collision operators, although preserving the mass balance, do not support the necessary symmetry constraints of the momentum equation in the standard lattices of LBM [73,93].

Remark 4. In any case, if we take $\delta_{y'}$ to handle arbitrary wall-lattice orientations, a way to determine this parameter is to measure the distance from the boundary node to the wall along its normal direction, and then to set this value for all wall cut links q. This was probably the strategy followed in [56] (which we will adopt throughout the rest of this work when referring to [56]). Yet, even using this approximation, these CK schemes hold critical limitations at arbitrary $\delta_{y'} \in [0,1]$. According to Table III, we see that the calibration parameter r, which parametrizes the coefficients in Eq. (16), turns out to be singular if $(3\nu - C_1\lambda_\Theta) + (\delta_{y'} - 1/2) = 0$. For example, close to the no-slip limit (where $C_1\lambda_\Theta \ll 1$), this singularity is found at $\delta_{y'} = 1 - \tau$, a result conceivable to happen in a typical parameter range. Although no reference was given to this defect in the original contribution [56], it is possible to identify it in Eq. (29) of [56]. In fact, Appendix B proves that our DBB solutions for r and Λ, respectively, given in Tables III and IV, recover the solutions given in Eq. (29) of [56].

Remark 5. On top of the above limitations, the prescription of the slip velocity condition established by any of the aforementioned "kinetic" schemes is impacted by angular-dependent errors. The anisotropy effect plaguing Eq. (17) is identified in the α^- coefficient and is given by $(3\Theta^2 - 1)/3\Theta^2$. Its functional form is identical to the no-slip BB rule [Eq. (20)] since this kind of artifact is intrinsic to low-order boundary schemes [63,94,97,103,112]. Even in the simplest lattice-aligned case, it renders the Λ calibration dependent on the wall orientation (a result not considered in [56]). For example, with the TRT collision and $\delta_{y'} = \frac{1}{2}$, as given in Table IV, we have $\Lambda = \frac{3}{2}(\frac{1}{8} + C_2\lambda^2)$ in a horizontal channel ($\Theta^2 = 1$) and $\Lambda = 3(\frac{1}{8} + 2C_2\lambda^2)$ in a diagonal channel ($\Theta^2 = \frac{1}{2}$).

Remark 6. Despite all defects, we note the existence of attempts [48,56,80] to extend these "kinetic" schemes to support generic lattice-wall discretizations, e.g., as sketched in Fig. 1(b), based on the interpolation of the CK schemes discussed above, such as CBBSR [48,80] or DBB [56]. It turns out that the construction of such interpolation-based strategies in the modeling of the slip velocity condition requires particular attention, specifically in the consideration of the discrete effects in r and Λ within the interpolation coefficients [56]. This is a nontrivial task and, as previously explained, may not even be possible to be satisfied in general wall-lattice configurations. The recognition of these limitations motivated us to follow an alternative "nonkinetic" route, based on the multireflection framework, in order to construct consistent LBM slip schemes, which will be addressed in Secs. V and VI.

Comment on bounce back (BB) as slip velocity boundary scheme

As previously mentioned, the general update rule of CK scheme (16) reduces to the bounce-back (BB) rule when setting $\mathcal{A} = 1$, $\mathcal{D} = 2$, and $\mathcal{B} = \mathcal{C} = 0$, which gives $f_{\bar{q}}(\vec{x}_b, t+1) = \tilde{f}_q(\vec{x}_b, t) + 2j_{\bar{q}\,w}(\vec{x}_w, t)$. In the same fashion, the BB closure relation follows as a particular case of the closure relation of the general CK schemes by setting $\sigma = 0$ in $\alpha^\pm$ coefficients of Eq. (17). Its form is given by Eq. (20), where we refer to [63,64,67,94,112,113] or the textbook [37] for a step by step derivation of the BB closure relation. Below, the sign $\mp$ in α^+ depends on whether a bottom or top wall is considered:

$$u_{x'} \mp \alpha^+ \partial_{y'} u_{x'} + \alpha^- \partial_{y'}^2 u_{x'} = U_w{}',$$
$$\alpha^+ = \frac{1}{2}, \quad \alpha^- = \frac{3\Theta^2 - 1}{3\Theta^2}\Lambda. \tag{20}$$

Although the BB rule was originally developed to model no-slip walls, its utilization as slip model can be found in numerous works: from early contributions [82,88–91] to more recent efforts [80,87,101,102]. As of today, the slip velocity condition satisfied by BB remains the subject of continuous debate, where its validity has been either advocated [80,102,114] or refuted [51,115–117]. The reason is that, even though the BB closure relation may recover the correct slip coefficients [Eq. (13)] via the single tuning parameter Λ [which controls α^- as shown in Eq. (20)], the underlying calibration procedure is artificial (because it will depend on grid resolution to indirectly alter α^+, an issue with no parallel for no-slip walls at $\delta_{y'} = \frac{1}{2}$) and it lacks generality (because this kind of Λ calibration is only successful for lattice-aligned channels, although this limitation is also present in the no-slip case). An additional aspect is that the Λ calibration is collision model dependent, as summarized in Table V. In this context, we note that the BB calibrations presented in Table V assume a halfway wall location, i.e., $\delta_{y'} = \frac{1}{2}$. While it is possible to extend these calibrations to arbitrary $\delta_{y'} \in [0,1]$, this practice is not explored here. At last, we note that, similarly to the no-slip case [112], the utilization of the BB rule as slip model holds the (second-order) anisotropy defects, which are identified through the Θ^2 terms in α^- of Eq. (20).

TABLE V. Calibration of the BB rule [Eq. (20)] to match Eq. (13) for a lattice-aligned (horizontal or diagonal) channel flow with $\delta_{y'} = \frac{1}{2}$. The calibration differs along the three families of collision operators: TRT, REG/S-REG, and BGK schemes. Note that $\widetilde{\alpha}^- = \left(\frac{3\Theta^2}{3\Theta^2-1}\right)\left(\frac{1}{8} + \frac{1}{2}C_1\lambda_\Theta H + C_2\lambda_\Theta^2\right)$, with $\lambda_\Theta = \lambda/\Theta$.

	TRT	REG/S-REG	BGK
ν	$\forall\,\mathbb{R}^+$	$\frac{2}{3}\widetilde{\alpha}^-$	$\frac{1}{3}\sqrt{\widetilde{\alpha}^-}$
Λ	$\widetilde{\alpha}^-$	$\frac{3}{2}\nu$	$9\nu^2$

V. LINEAR SLIP VELOCITY BOUNDARY SCHEMES AND THEIR CALIBRATION

This section introduces a class of *linear* linkwise slip velocity boundary schemes. They are designed to follow a closure relation in accordance to Eq. (13). These linear slip schemes have the advantage of operating locally, i.e., on a single node, but the disadvantage of retaining some calibration requirements and/or operation limitations. While both these negative aspects are shared with the "kinetic" schemes discussed in Sec. IV, the interest behind our proposed "one-point" slip schemes is that they provide a simpler framework to search for possible improvements, which will be explored at the end of the section via specific calibration strategies.

The linear (LI) scheme considered herein follows the works [64,67], originally formulated for no-slip wall conditions. Here, we extend them to the slip-flow regime. The LI scheme operates on the boundary node $\vec{x}_\mathrm{b}$, where $\vec{x}_\mathrm{b} + \vec{c}_q$ is a solid node, according to the update rule

$$f_{\bar{q}}(\vec{x}_\mathrm{b},t+1) = \kappa_1 \tilde{f}_q(\vec{x}_\mathrm{b},t) + \bar{\kappa}_{-1}\tilde{f}_{\bar{q}}(\vec{x}_\mathrm{b},t) + \kappa_0 f_q(\vec{x}_\mathrm{b},t+1) + F_q^{p.c.}(\vec{x}_\mathrm{b},t) - \alpha^{(u)} j_{q\,w}(\vec{x}_w,t), \tag{21}$$

where $\{\kappa_1,\bar{\kappa}_{-1},\kappa_0\}$ denote interpolation coefficients given in Table VI. In order to keep the implementation local, the κ_0 population is evaluated after the propagation step. The other terms in Eq. (21) have the following meaning: $F_q^{p.c.} = (1-\kappa_1)g_q^-$ is a local post-collision correction and $j_{q\,w} = t_q\rho_0(\vec{U}_w\cdot\vec{c}_q)$ prescribes the wall momentum (vanishing for a resting wall). The prefactor $\alpha^{(u)}$ plays a parametrization role in the scheme structure [64].

Table VI summarizes the parameters featuring in the three LI interpolation strategies considered herein, namely, central linear interpolation (CLI), upwind and downwind linear interpolation (MGULI and MGDLI); they are denoted with the suffix "slip" to differentiate them from the standard no-slip schemes [64]. The two are matched at the no-slip velocity limit. In fact, the new LI slip schemes can be derived from the original LI no slip by substituting the parameter δ_q in the no-slip case by α_q^+ to reproduce the slip case, e.g., compare Table VI in this work against Table 3 in [64] or Table 4 in [94]. In terms of characteristics we note that, while CLI slip, MGULI slip and MGDLI slip are expected to differ in a number of properties (e.g., in transient solutions, staggered invariants, convergence and stability characteristics), they share identical steady-state solutions. Overall, the class of linear slip schemes satisfy the following steady-state closure relation:

$$j_q(\vec{x}_\mathrm{b}) + \alpha_q^+\partial_q j_q(\vec{x}_\mathrm{b}) + \alpha_q^-\partial_q^2 j_q(\vec{x}_\mathrm{b}) = j_{q\,w}(\vec{x}_w),$$
$$\alpha_q^+ = (\delta_q + C_1\lambda_q), \quad \alpha_q^- = \frac{3\Theta_q^2-1}{3\Theta_q^2}\Lambda, \quad \lambda_q = \frac{\lambda}{\Theta_q}. \tag{22}$$

Compared to the target closure relation [Eq. (13)] we notice that the α_q^+ coefficient in Eq. (22) is correctly imposed. However, the α_q^- coefficient displays the same deficient structure identified in BB [Eq. (20)]. The calibration of the α_q^- coefficient is therefore mandatory. Below, we suggest two calibration strategies to fix this limitation and set the linear-slip schemes consistent with Eq. (13). It is important to note that these strategies are only applicable to the particular case of streamwise invariant channel flows. For more general flows, a linkwise boundary scheme supporting a structural parabolic accuracy must be used, which will be the subject of Sec. VI.

TABLE VI. Coefficients of linear link-wise slip velocity boundary schemes (LI-slip) for Eq. (21) with $\alpha_q^+ = (\delta_q + C_1\lambda_q)$. The operation limits in each scheme are: $\alpha_q^+ \geqslant 0$ in CLI slip, $0 \leqslant \alpha_q^+ \leqslant \frac{1}{2}$ in MGULI slip, and $\alpha_q^+ \geqslant \frac{1}{2}$ in MGDLI slip. The post-collision correction is $F_q^{p.c.} = (1-\kappa_1)g_q^-$ (thereby, in CLI slip $F_q^{p.c.} = 0$).

	CLI slip	MGULI slip	MGDLI slip
κ_1	1	$2\alpha_q^+$	$\frac{1}{2\alpha_q^+}$
κ_0	$\frac{1-2\alpha_q^+}{1+2\alpha_q^+}$	$1-\kappa_1$	0
$\bar{\kappa}_{-1}$	$-\kappa_0$	0	$1-\kappa_1$
$\alpha^{(u)}$	$\frac{4}{1+2\alpha_q^+}$	2	$\frac{1}{\alpha_q^+}$

A. Calibrating the TRT free collision parameter Λ

The first strategy consists of setting $\Lambda = (\frac{3\Theta_q^2}{3\Theta_q^2-1})\tilde{\alpha}_q^-$, where $\tilde{\alpha}_q^- = (\frac{\delta_q^2}{2} + C_1\lambda_q\delta_q + C_2\lambda_q^2)$, so that $\tilde{\alpha}_q^-$ has the same form of α_q^- in Eq. (13). This effectively makes Eq. (22) to match Eq. (13). Yet, for the reasons explained in Remark 3 of Sec. IV, we recall that Λ must be held linkwise constant, which implies the linkwise varying parameters featuring in Λ must be constant as well, i.e., $\delta_q = \delta_y$ and $\Theta_q = \Theta$. This explains why the effective use of any Λ-based strategy is limited to *lattice-aligned* plane boundaries (differently from what seems to be suggested in [56]).

B. Calibrating the effective wall to boundary-node linkwise distance

The second strategy maintains Λ as a free parameter and adopts the redefinition $\delta_q \to \tilde{\delta}_q$. The idea is the following: rather than considering δ_q in the original formulas as the parameter that measures the linkwise distance from $\vec{x}_\mathrm{b}$ to the wall location $\vec{x}_w$ (see Fig. 2), we replace it by $\tilde{\delta}_q = r_q - \frac{1}{(r_q-H_q/2)}(\tilde{\alpha}_q^- - \frac{3\Theta_q^2-1}{3\Theta_q^2}\Lambda)$, where $\tilde{\alpha}_q^- = (\frac{r_q^2}{2} + C_1\lambda_q r_q + C_2\lambda_q^2)$ and r_q measures the linkwise distance from the lattice-projected boundary node $x_{q\mathrm{b}} = \vec{x}_\mathrm{b}/\Theta_q$ to the lattice-projected wall point $H_q = H/\Theta_q$, whereby $r_q = x_{q\mathrm{b}} + H_q/2$. For more details on the meaning of these parameters, we refer to [67] (specifically, to see the comprehensive example given in Sec. 2.4.1 of [67]). The advantage of this second strategy is that it is not limited to lattice-aligned configurations. Interestingly,

it enables the local LI scheme to support *exact* Poiseuille flow solutions in the slip-flow regime for arbitrarily oriented channels, $\forall\ \Lambda$. This constitutes an affordable way to simulate microchannel gaseous flows in the slip-flow regime (although limited to channel-like geometries).

VI. PARABOLIC SLIP VELOCITY BOUNDARY SCHEMES

This section introduces a class of *parabolic* linkwise slip velocity boundary schemes, whose closure relation *exactly* reproduces Eq. (13). Furthermore, the schemes here proposed support non-mesh-aligned walls for general planar configurations, without any calibration requirement, i.e., only physical parameters are used as input. To formulate these parabolic-slip schemes we adopt the multireflection (MR) [63,64,94,113] framework. The downside of this procedure is that it operates nonlocally according to a two-node implementation. Nonetheless, we note that alternative routes exist to do the same task locally, e.g., [97], although at the expense of an increased complexity in formulation.

The methodology to construct MR schemes is explained in a series of works, e.g., [63,64]. We refer to them for details on the derivation of MR schemes. Succinctly, the idea consists of determining a suitable linear combination of post-collision quantities (whose structure is detailed below), so that the microscopic closure relation reproduced by the LBM boundary scheme (e.g., determined via Chapman-Enskog analysis) approximates, in the Taylor-series sense, the intended macroscopic boundary condition, up to some prescribed order, here taken as $\mathcal{O}(\epsilon^3)$. In the present case, the closure relation of the boundary condition to be sought is given by Eq. (13).

The general class of MR schemes here considered is based on the works [64,67], originally formulated for no-slip wall conditions, which we extend to the slip-flow regime. The MR scheme operates in a linkwise fashion on the pair of grid nodes $\{\vec{x}_{\rm b},\vec{x}_{\rm b}-\vec{c}_q\}$, where $\vec{x}_{\rm b}+\vec{c}_q$ is a solid node, based on the update rule

$$\begin{aligned} f_{\bar{q}}(\vec{x}_{\rm b},t+1) =& \kappa_1 \tilde{f}_q(\vec{x}_{\rm b},t) + \bar{\kappa}_{-1}\tilde{f}_{\bar{q}}(\vec{x}_{\rm b},t) + \kappa_0 f_q(\vec{x}_{\rm b},t+1) \\ &+ \kappa_{-1} f_q(\vec{x}_{\rm b}-\vec{c}_q,t+1) + \bar{\kappa}_{-2}\tilde{f}_{\bar{q}}(\vec{x}_{\rm b}-\vec{c}_q,t) \\ &+ F_q^{p.c.}(\vec{x}_{\rm b},t) - \alpha^{(u)} j_{q\,w}(\vec{x}_w,t), \end{aligned} \tag{23}$$

where $\{\kappa_1,\kappa_0,\bar{\kappa}_{-1},\kappa_{-1},\bar{\kappa}_{-2}\}$ denote interpolation coefficients given in Table VII. Note that, in order to reduce the span of grid nodes from three to two, the κ_0 and κ_{-1} populations are evaluated after the propagation step. The meaning of the parameters $F_q^{p.c.}$, $j_{q\,w}$, and $\alpha^{(u)}$ in Eq. (23) was explained in Sec. V; they have the same meaning here, although possessing different content.

Table VII summarizes the solution for $\{\kappa_1,\kappa_0,\bar{\kappa}_{-1},\kappa_{-1},\bar{\kappa}_{-2}\}$, $\alpha^{(u)}$, and $F_q^{p.c.}$ in the general MR(k) family and the two particular cases MR1 and MGMR(C) subfamilies for the slip regime. Note that k is a general parameter that can be set to recover MR1 or MGMR(C) schemes as follows: $k=(-\frac{1}{2}+\alpha_q^+ +\alpha_q^-)$ in MR1 and $k=(-\frac{1}{2}+\alpha_q^+ +\alpha_q^- - C\Lambda^-)$ in MGMR(C), where C and Λ^- are both free tunable. The role of these free parameters views primarily stability purposes. The similarities and differences among them are explained in more details in [64,67]. As pointed out in Sec. V, even though coefficients may differ, since they fulfill a similar steady closure relation (13), they yield identical steady solutions [up to $\mathcal{O}(\epsilon^3)$ accuracy in the Chapman-Enskog expansion]. Once again, we note that the parabolic-slip schemes derived herein are self-consistent, meaning that they recover the original parabolic no-slip schemes [63,64] at the no-slip velocity limit. As a matter of fact, we point out that these MR slip schemes are readily derived from the original MR no-slip ones [63,64] by performing the following model transformations: $\delta_q \to \alpha_q^+$ and $\delta_q^2 \to 2\alpha_q^-$; a confirmation of this equivalency follows by comparing Table VII of this work against Table 3 of [64].

TABLE VII. Coefficients of parabolic multi-reflection linkwise slip velocity boundary schemes (MR-slip) for Eq. (23) with $\alpha_q^+=(\delta_q+C_1\lambda_q)$ and $\alpha_q^-=(\frac{\delta_q^2}{2}+C_1\lambda_q\delta_q+C_2\lambda_q^2)$, where $\alpha_q^+\geqslant 0$ and $\alpha_q^-\geqslant 0$ as operation limits for all schemes. The post-collision correction is $F_q^{p.c.}=\alpha^{(u)}\Lambda^-(g_q^- - F_q)$.

	MR(k) slip	MR1 slip	MGMR(C) slip
κ_1	$\frac{2\alpha_q^+ +2\alpha_q^- -k}{1+k}$	1	$\frac{1+2\alpha_q^+ +2\alpha_q^- +2C\Lambda^-}{1+2\alpha_q^+ +2\alpha_q^- -2C\Lambda^-}$
κ_0	$\frac{\frac{3}{2}-3\alpha_q^+ -4\alpha_q^- +2k}{1+k}$	$\frac{1-2\alpha_q^+ -4\alpha_q^-}{1+2\alpha_q^+ +2\alpha_q^-}$	$\frac{1-2\alpha_q^+ -4\alpha_q^- -4C\Lambda^-}{1+2\alpha_q^+ +2\alpha_q^- -2C\Lambda^-}$
$\bar{\kappa}_{-1}$	$\frac{\frac{1}{2}-\alpha_q^+ +2k}{1+k}$	$-\kappa_0$	$\frac{-1+2\alpha_q^+ +4\alpha_q^- -4C\Lambda^-}{1+2\alpha_q^+ +2\alpha_q^- -2C\Lambda^-}$
κ_{-1}	$\frac{-\frac{1}{2}+\alpha_q^+ +2\alpha_q^- -k}{1+k}$	$\frac{2\alpha_q^-}{1+2\alpha_q^+ +2\alpha_q^-}$	$\frac{2\alpha_q^- +2C\Lambda^-}{1+2\alpha_q^+ +2\alpha_q^- -2C\Lambda^-}$
$\bar{\kappa}_{-2}$	$\frac{-\frac{1}{2}+\alpha_q^+ -k}{1+k}$	$-\kappa_{-1}$	$\frac{-2\alpha_q^- +2C\Lambda^-}{1+2\alpha_q^+ +2\alpha_q^- -2C\Lambda^-}$
$\alpha^{(u)}$	$\frac{2}{1+k}$	$\frac{4}{1+2\alpha_q^+ +2\alpha_q^-}$	$\frac{4}{1+2\alpha_q^+ +2\alpha_q^- -2C\Lambda^-}$

VII. BENCHMARK RESULTS: STEADY POISEUILLE GAS FLOW IN SLIP-FLOW REGIME

The steady Poiseuille gas flow, developing in the slip-flow regime, will be used as benchmark to numerically validate the performance of the LBM slip boundary schemes introduced in Secs. IV, V, and VI. Typically, the study of this problem is focused on two features: (i) the wall slip on the velocity profile and (ii) the minimum in the mass flow rate as function of Kn, the so-called Knudsen's paradox. This section focuses on the quality and the accuracy of the numerical velocity profiles.

For simulations we adopt specific values for the pair of slippage coefficients C_1 and C_2 (although we note that other C_1 and C_2 values do *not* affect conclusions, as will be illustrated at the end of Sec VIII). The zeroth-order (no-slip) condition considers $C_1=C_2=0$. The first-order slip velocity model adopts Maxwell's slip theory [15], which sets $C_1=1.0$ and $C_2=0$. The second-order slip velocity model uses the values due to Cercignani [21]: $C_1=1.1466$ and $C_2=0.9576$, derived through numerical solutions of the continuous Boltzmann-BGK equation for an isothermal gas flow at low Kn. The channel flow is driven by a body force mechanism $F_x=0.01$ (simulation units). A pressure gradient could be applied instead, and would produce identical results, except for the "kinetic" schemes discussed in Remark 2 of Sec. IV; further comments on this issue are given at the end of this section. The density ground state is always set to $\rho_0=1$ (simulation units). The convergence of numerical solutions is determined by the steady-state criterion, measured by the relative change of the mean velocity $\langle u_x\rangle$ (numerically computed with the midpoint

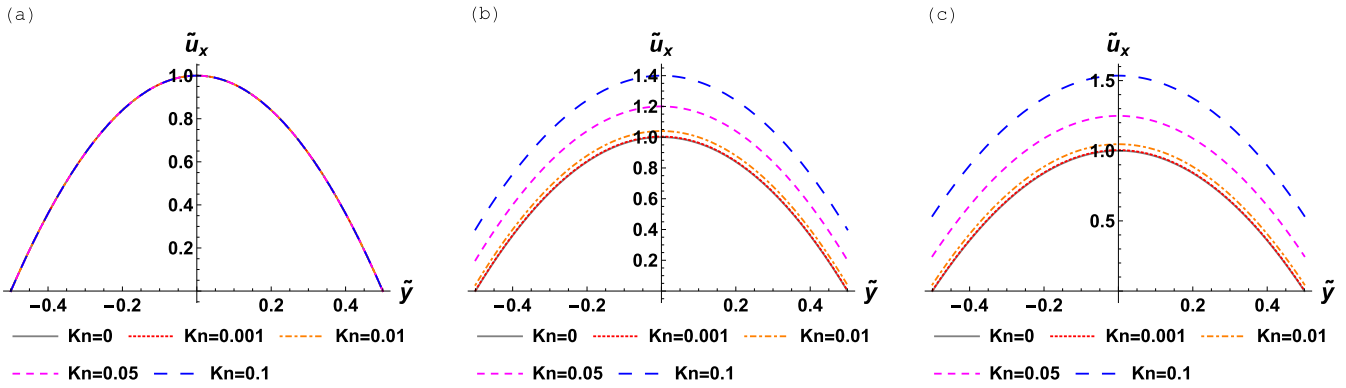

FIG. 3. Poiseuille flow velocity solutions at different Kn numbers within slip-flow theory [Eq. (24)]. (a) No-slip velocity boundary condition ($C_1 = C_2 = 0$). (b) First-order slip velocity boundary condition ($C_1 = 1.0$ and $C_2 = 0$ by Maxwell [15]). (c) Second-order slip velocity boundary condition ($C_1 = 1.1466$ and $C_2 = 0.9576$ by Cercignani [21]).

rule) not superior to 10^{-12}, measured after 100 consecutive time steps, i.e., $|\frac{\langle u_x\rangle(t)}{\langle u_x\rangle(t-100)} - 1| \leqslant 10^{-12}$.

The numerical tests cover all boundary schemes introduced in Secs. IV, V and VI. For the LBM collision operator we choose the TRT model, although results are readily applicable to other collision models, such as REG/S-REG and BGK, providing the different meaning of Λ is accounted for (see Table II and discussion in Appendix A). We recall that in MRT and TRT the Λ parameter is free tunable and ν independent, while in collision models such as REG/S-REG and BGK the $\Lambda(\nu)$ dependency is unavoidable, meaning the fluid viscosity ν is the effective simulation calibration parameter. Such a viscosity calibration is a common practice in LBM, e.g., [100,102,118–121], although it suffers from several pitfalls as debated in [63,64,93,94,115,117,120].

Concerning the physical parametrization of the problem, we note that, in the slip-flow regime, the nondimensional group Kn only applies at boundaries where its value determines the amount of slip experienced by the fluid velocity with respect to the wall velocity. The Knudsen number is defined as $\mathrm{Kn} = \lambda/H$, where H measures a characteristic length scale (in simulation units) and the mean-free path λ is a free parameter since the viscosity and mean-free-path relationship is not used herein (such a relationship is a superfluous constraint in the slip-flow regime as explained in Remark 1 of Sec. IV).

A. Analytical velocity profile

Consider the steady and unidirectional $\vec{u} = \{u_x, 0\}$ (force-driven) Poiseuille flow bounded by resting walls ($U_w = 0$). The fluid-wall interaction is modeled with the second-order slip velocity condition. With these conditions, the normalized exact solution of the velocity profile $\tilde{u}_x^{(\mathrm{exact})}$ is given by

$$\tilde{u}_x^{(\mathrm{exact})} = 1 - 4\tilde{y}^2 + 4C_1\mathrm{Kn} + 8C_2\mathrm{Kn}^2, \quad \tilde{y} = \frac{y}{H} \in \left[-\frac{1}{2}, \frac{1}{2}\right],$$
$$\tilde{u}_x^{(\mathrm{exact})} = \frac{u_x^{(\mathrm{exact})}}{u_0}, \quad u_0 = \frac{F_x H^2}{8\nu\rho_0}, \quad \mathrm{Kn} = \frac{\lambda}{H}, \tag{24}$$

where H denotes the channel width and u_0 corresponds to the centerline velocity of the no-slip solution.

Figure 3 shows the velocity profiles given by Eq. (24), displayed in the following three regimes of wall slip conditions: (a) no slip ($C_1 = C_2 = 0$), (b) first-order slip ($C_1 = 1.0$ and $C_2 = 0$ by Maxwell [15]), and (c) second-order slip ($C_1 = 1.1466$ and $C_2 = 0.9576$ by Cercignani [21]). Irrespective of the Kn number, we note that the ensemble of velocity solutions corresponds to the linear superposition of a parabola and a constant value of slip at boundaries [117]. Given that in bulk the LBM equation *exactly* captures the parabolic profile (a result pointed out in many past studies, e.g., [63,67,93,97,112,122]), then any inaccuracy within this problem must be caused by the boundary scheme. It turns out that the nature of boundary errors differs depending on whether the channel walls are parallel or oblique to the lattice links. Therefore, we will discuss these two cases separately below.

B. LBM velocity profile in lattice-aligned horizontal channel

The *exact* solution of the LBM scheme in this problem, considering a lattice-aligned horizontal channel (i.e., $\Theta_q = \Theta = 1$), is given by Eq. (25a) in bulk and Eq. (25b) on boundary nodes:

$$F_x + \nu\rho_0\partial_y^2 u_x = 0 \quad \text{for } y \in \left]-\frac{N_y}{2} + \frac{1}{2}, \frac{N_y}{2} - \frac{1}{2}\right[, \tag{25a}$$
$$u_x \mp \alpha^+\partial_y u_x + \alpha^-\partial_y^2 u_x\big|_{y_\mathrm{b} = \mp\frac{N_y}{2} \pm \frac{1}{2}} = 0. \tag{25b}$$

Note that the Taylor-type boundary condition (25b) is written with generic coefficients $\alpha^\pm$ that are summarized (in nondimensional form) in Table VIII, where boundary nodes $y_\mathrm{b} = \mp\frac{N_y}{2} \pm \frac{1}{2}$ lie adjacent to bottom and top walls, respectively, and N_y denotes the number of grid nodes resolving the channel width [Fig. 2(a)]. By introducing $\delta_y \in [0,1]$ as the distance between the channel walls and the boundary nodes, the effective channel width is defined as $H = N_y + 2\delta_y - 1$ [Fig. 2(a)]. Then, the normalized LBM solution, obtained by solving Eq. (25a) subject to Eq. (25b), is given by

$$\tilde{u}_x = 1 - 4\tilde{y}^2 + 4\epsilon(\alpha^+ - \delta_y) + 8\epsilon^2\left(\frac{1}{2}\delta_y^2 - \delta_y\alpha^+ + \alpha^-\right),$$
$$\tilde{y} = \frac{y}{H} \in \left[-\frac{1}{2}, \frac{1}{2}\right], \tag{26}$$
$$\tilde{u}_x = \frac{u_x}{u_0}, \quad u_0 = \frac{F_x H^2}{8\nu\rho_0}, \quad \epsilon = \frac{1}{H}.$$

TABLE VIII. Coefficients in the closure relations of each LBM slip boundary scheme considered in the horizontal channel case. TRT model is considered herein (the conversion to other collision models follows from Table II).

	α^+	α^-
BB scheme [Eq. (20)]	$\frac{1}{2}$	$\frac{2}{3}\Lambda$
CK scheme [Eq. (17) with Eq. (18)]	$\frac{1}{2}+C_1(\mathrm{Kn}/\epsilon)$	$\frac{2}{3}\Lambda+\frac{1}{2}C_1(\mathrm{Kn}/\epsilon)$
LI slip scheme [Eq. (22)]	$\delta_y+C_1(\mathrm{Kn}/\epsilon)$	$\frac{2}{3}\Lambda$
MR slip scheme [Eq. (13)]	$\delta_y+C_1(\mathrm{Kn}/\epsilon)$	$\frac{1}{2}\delta_y^2+C_1(\mathrm{Kn}/\epsilon)\delta_y+C_2(\mathrm{Kn}/\epsilon)^2$

Since the only error source comes from boundaries, the difference between numerical [Eq. (26)] and exact [Eq. (24)] solutions provides a measure for the artificial (numerical) slip:

$$\Delta\tilde{u}_x=\tilde{u}_x-\tilde{u}_x^{(\mathrm{exact})}=4\epsilon[\alpha^+-\delta_y-C_1(\mathrm{Kn}/\epsilon)]+8\epsilon^2\left[\tfrac{1}{2}\delta_y^2-\delta_y\alpha^++\alpha^--C_2(\mathrm{Kn}/\epsilon)^2\right]. \quad (27)$$

Note, the terms embodying the "physical" slip shall not vanish as $\epsilon\to 0$. Hence, they are absent from $\Delta\tilde{u}_x$, which retains numerical errors only. The overall velocity error, measured with respect to the exact analytical solution [Eq. (24)], is computed as the sum over all nodal points y_i with $i=1,\ldots,N_y$:

$$|\mathcal{E}(\tilde{u}_x)|=\left|\frac{\sum_i\Delta\tilde{u}_x(y_i)}{\sum_i\tilde{u}_x^{(\mathrm{exact})}(y_i)}\right|. \quad (28)$$

Based on Eq. (27) and the $\alpha^\pm$ coefficients summarized in Table VIII, it is direct to determine the dependence of the normalized numerical slip on the grid resolution $\epsilon=1/H$ and, accordingly, to compute the accuracy measure given by $|\mathcal{E}(\tilde{u}_x)|$. We note that in the horizontal channel case, the error $\Delta\tilde{u}_x$ is constant along the nodal points y_i. The only error source is the numerical slip at the wall, which leads to a uniform shift in the velocity profile from the correct values. A different scenario occurs for non-mesh-aligned walls, where the velocity profile gets distorted everywhere. This will be illustrated in the inclined channel case (Sec. VII C). For now, let us focus on the lattice-aligned case and discuss the scaling of the numerical slip error with grid resolution: (i) by theoretically analyzing the three different physical models of wall slippage, and (ii) by verifying the theoretical conclusions against numerical tests.

The *no-slip* flow condition is recovered in limits of (i) $\mathrm{Kn}=0\ \forall\ \{C_1,C_2\}$ or (ii) $C_1=C_2=0\ \forall\ \mathrm{Kn}$. Here, CK reduces to BB, with $\alpha^+=\frac{1}{2}$ in both cases. Hence, if $\delta_y\neq\frac{1}{2}$, then a first-order slip artifact is introduced, given by $\Delta\tilde{u}_x=\epsilon(2-4\delta_y)+\mathcal{O}(\epsilon^2)$. Otherwise, with $\delta_y=\frac{1}{2}$ only a second-order slip artifact appears: $\Delta\tilde{u}_x=\epsilon^2\left(\frac{16}{3}\Lambda-1\right)$, which vanishes for the well-known relaxation choice $\Lambda=\frac{3}{16}$ [63,67,93,112]. Most generally, a calibration of the kind $\Lambda(\delta_y)$ with $\forall\ \delta_y\in[0,1]$ can also be constructed through an artificial resolution-dependent tuning (refer to [63,67,93] for more details). The LI slip schemes produce a similar second-order slip error: $\Delta\tilde{u}_x=\epsilon^2\left(\frac{16}{3}\Lambda-4\delta_y^2\right)$, which vanishes for the well-known relaxation choice $\Lambda=\frac{3}{4}\delta_y^2$, $\forall\ \delta_y\in[0,1]$ [67,93]. Finally, the MR slip (parabolic) schemes retrieve the exact solution with $\Delta\tilde{u}_x=0$, $\forall\ \delta_y\in[0,1]$ and $\forall\ \Lambda\in\mathbb{R}^+$.

The *first-order* slip-flow condition is recovered for $\mathrm{Kn}>0$ with $C_1\neq 0$ and $C_2=0$. In this case, differences between CK and BB appear already at the first order. In order to make the first-order error to vanish, i.e., $\Delta\tilde{u}_x=4\epsilon[\alpha^+-\delta_y-C_1(\mathrm{Kn}/\epsilon)]+\mathcal{O}(\epsilon^2)$, the BB needs to consider a resolution-dependent parameter H in the Λ calibration, while CK schemes require the σ calibrations given by Eq. (18) for $\delta_y=\frac{1}{2}$ or by Eq. (19) for $\delta_y\in[0,1]$. The vanishing of the second-order slip error in CK schemes at $\delta_y=\frac{1}{2}$ requires setting $\Lambda=\frac{3}{16}$ (while for $\delta_y\in[0,1]$ the Λ calibration is given in Table IV). The LI slip schemes, if not properly calibrated, retain the first-order slip error $\Delta\tilde{u}_x=-8\epsilon\delta_yC_1\mathrm{Kn}+\mathcal{O}(\epsilon^2)$. According to the calibration strategies presented in Sec. V, the relaxation choice $\Lambda=\frac{3}{2}C_1\delta_y(\mathrm{Kn}/\epsilon)$ places the LI slip scheme second-order accurate. The vanishing of the second-order error requires the full calibration $\Lambda=\frac{3}{2}[\frac{\delta_y^2}{2}+C_1\delta_y(\mathrm{Kn}/\epsilon)]$, which retrieves the exact solution [Eq. (24)] for $\delta_y\in[0,1]$. Finally, the MR slip schemes guarantee, once again, the exact solution with $\Delta\tilde{u}_x=0$, $\forall\ \delta_y\in[0,1]$ and $\forall\ \Lambda\in\mathbb{R}^+$.

The *second-order* slip-flow condition is recovered for $\mathrm{Kn}>0$ with $C_1\neq 0$ and $C_2\neq 0$. As expected, the CK and BB schemes differ. However, the two cases exhibit a zeroth-order slip error $\Delta\tilde{u}_x=-8C_2\mathrm{Kn}^2+\mathcal{O}(\epsilon)$, even setting $\delta_y=\frac{1}{2}$ and σ properly calibrated in the first-order coefficient of CK schemes. That is, the second-order coefficient has a leading-order impact on the scheme accuracy. Assuming $\delta_y=\frac{1}{2}$ with $\Lambda=\frac{3}{2}C_2(\mathrm{Kn}/\epsilon)^2$ sets CK schemes second-order accurate, but conserves the slip error $\Delta\tilde{u}_x=\epsilon^2(\frac{16}{3}\Lambda-1)$. The vanishing of the full slip error, i.e., $\Delta\tilde{u}_x=\epsilon^2[\frac{16}{3}\Lambda-1-8C_2(\mathrm{Kn}/\epsilon)^2]$, requires accounting for $\delta_y=\frac{1}{2}$ in the Λ calibration, i.e., $\Lambda=\frac{3}{2}[(\frac{1}{2})^3+C_2(\mathrm{Kn}/\epsilon)^2]$. The elimination of slip errors in BB requires a grid-dependent Λ calibration as summarized in Table V. The LI slip schemes are also plagued by the zeroth-order error $\Delta\tilde{u}_x=-8C_2\mathrm{Kn}^2+\mathcal{O}(\epsilon)$, when they are not properly calibrated. We note that the calibration previously used to remove the numerical slip for the case $C_1\neq 0$ and $C_2=0$, i.e., $\Lambda=\frac{3}{2}C_1\delta_y(\mathrm{Kn}/\epsilon)$, leads to no improvements here since it conserves the zeroth-order error now placed by $C_2\neq 0$, i.e., $\Delta\tilde{u}_x=-8C_2\mathrm{Kn}^2+\mathcal{O}(\epsilon)$. In order to eliminate the zeroth-order slip error we have to set $\Lambda=\frac{3}{2}C_2(\mathrm{Kn}/\epsilon)^2$, which effectively places the LI slip schemes as first-order accurate with respect to the second-order slip velocity condition. Since the slip error left as residue is $\Delta\tilde{u}_x=-8\epsilon\delta_yC_1\mathrm{Kn}+\mathcal{O}(\epsilon^2)$, the improvement to $\Delta\tilde{u}_x=\mathcal{O}(\epsilon^2)$ requires extending the calibration to $\Lambda=\frac{3}{2}[C_1\delta_y(\mathrm{Kn}/\epsilon)+C_2(\mathrm{Kn}/\epsilon)^2]$. The vanishing of the $\mathcal{O}(\epsilon^2)$ error, which remains due to the imprecise δ_y wall location, requires further expanding the calibration to $\Lambda=\frac{3}{2}[\frac{\delta_y^2}{2}+C_1\delta_y(\mathrm{Kn}/\epsilon)+C_2(\mathrm{Kn}/\epsilon)^2]$. With this Λ calibration the LI slip schemes lead to the exact analytical solution [Eq. (24)]. Finally, the MR slip schemes hold the exact parabolic solution

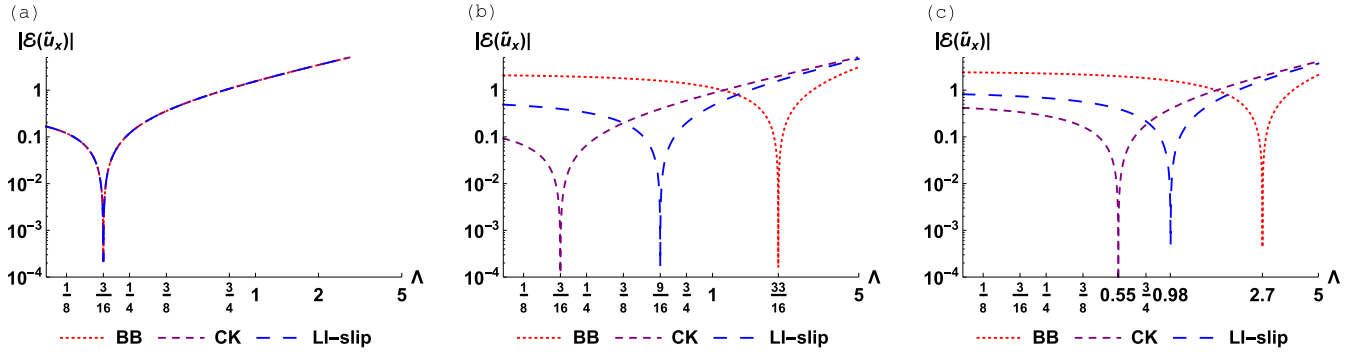

FIG. 4. Accuracy $|\mathcal{E}(\tilde{u}_x)|$ as function of relaxation parameter Λ. Note, the meaning of Λ may be either of a free parameter (MRT/TRT) or a viscosity-dependent one (REG/BGK) (see Table II). All cases refer to horizontal channel ($\Theta = 1$) with midway walls ($\delta_y = \frac{1}{2}$), resolved by $N = 5$ grid nodes along width, i.e., channel width $H = N - 1 + 2\delta_y = 5$ (simulation units). (a) No-slip flow regime (Kn $= 0$) where BB, CK, and LI slip schemes are exact at $\Lambda = \frac{3}{2}\frac{\delta_y^2}{2} = \frac{3}{16}$. (b) First-order slip-flow regime (Kn $= 0.1$, $C_1 = 1$, and $C_2 = 0$ [15]) where BB, CK, and LI slip schemes are exact at $\Lambda = \frac{3}{2}(\frac{\delta_y^2}{2} + C_1\lambda H) = \frac{33}{16}$, $\Lambda = \frac{3}{2}\frac{\delta_y^2}{2} = \frac{3}{16}$, and $\Lambda = \frac{3}{2}(\frac{\delta_y^2}{2} + C_1\lambda\delta_y) = \frac{9}{16}$, respectively. (c) Second-order slip-flow regime (Kn $= 0.1$, $C_1 = 1.1466$, and $C_2 = 0.9576$ [21]) where BB, CK, and LI slip schemes are exact at $\Lambda = \frac{3}{2}(\frac{\delta_y^2}{2} + C_1\lambda H + C_2\lambda^2) \simeq 2.70$, $\Lambda = \frac{3}{2}(\frac{\delta_y^2}{2} + C_2\lambda^2) \simeq 0.55$, and $\Lambda = \frac{3}{2}(\frac{\delta_y^2}{2} + C_1\lambda\delta_y + C_2\lambda^2) \simeq 0.98$, respectively. The MR slip schemes (not shown here) are exact $\forall$ slip-flow regimes and $\forall$ Λ.

with second-order slip conditions, guaranteeing $\tilde{u}_{\text{slip}} = 0$, $\forall\ \delta_y \in [0,1]$ and $\forall\ \Lambda \in \mathbb{R}^+$.

To illustrate with numerical results, the above discussions we report two studies below. Figure 4 shows the effect of the Λ calibration on the numerical slip magnitude $|\langle\Delta\tilde{u}_x\rangle|$, with grid resolution fixed. Figure 5 shows the effect of the grid resolution on the normalized error $|\mathcal{E}(\tilde{u}_x)|$, with Λ fixed, where convergence rates are quantified in Table IX. In the two cases, the most relevant simulation input parameters and outcomes are detailed in the figure captions. We note that all numerical results *exactly* agree with the theoretical findings, as predicted by Eq. (27) and Table VIII. Hence, the results confirm the importance of the Λ calibration on the low-order slip boundary schemes. As expected, the importance of the Λ calibration in correcting the errors from low-order slip schemes increases with the slip-flow condition order. For the correct modeling of the second-order slip-flow condition, this issue becomes of critical importance, implying the total lack of converge. The results from high-order MR slip (parabolic) schemes are not shown here since they recover the exact analytical solution [Eq. (24)], up to the machine accuracy, irrespective of Λ and H, for all cases.

Notwithstanding the defects previously identified, it should be borne in mind that this test corresponds to the most favorable simulation scenario. That is, wall discretization errors do *not* exist in this case. Hence, the next example will consider a more challenging test where the wall does not align with the uniform Cartesian lattice. That is, the wall discretization will introduce an additional error source. But, before addressing this case, we will finalize the section with a remark on the consideration of a pressure gradient, instead of a body force, in this class of problems.

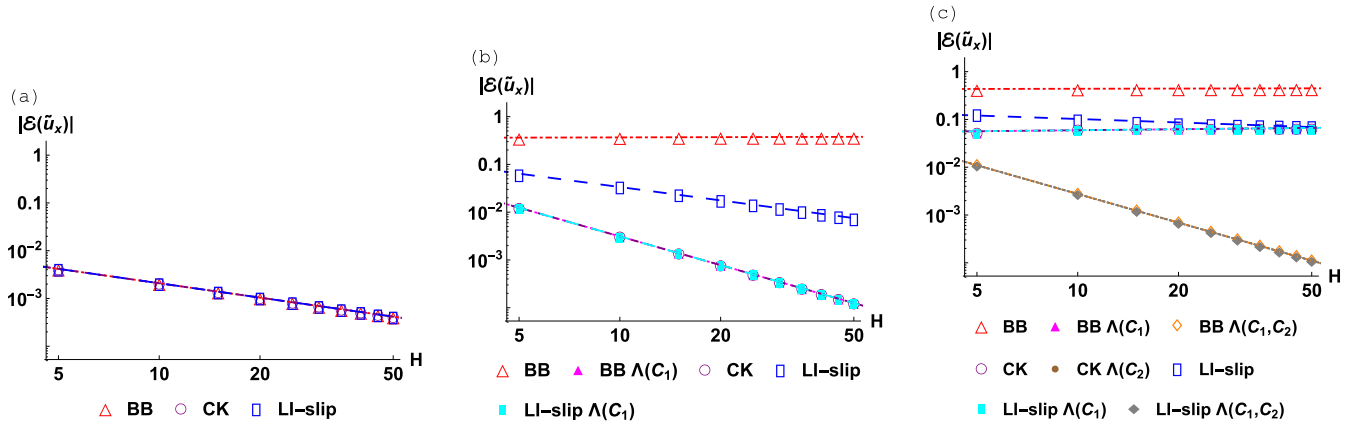

FIG. 5. Accuracy $|\mathcal{E}(\tilde{u}_x)|$ as function of grid resolution H. All cases refer to horizontal channel ($\Theta = 1$) with midway walls ($\delta_y = \frac{1}{2}$). Convergence rates are obtained through a linear regression, with the numerical values of slopes summarized in Table IX. Unless otherwise stated, the solutions are obtained for the fixed relaxation combination $\Lambda = \frac{1}{4}$. (a) No-slip flow regime (Kn $= 0$). (b) First-order slip-flow regime (Kn $= 0.1$, $C_1 = 1$, and $C_2 = 0$ [15]). (c) Second-order slip-flow regime (Kn $= 0.1$, $C_1 = 1.1466$, and $C_2 = 0.9576$ [21]). The MR slip schemes (not shown here) are exact for all slip-flow regimes, $\forall$ Λ values and $\forall$ H; hence, concept of grid convergence does not apply.

TABLE IX. Quantification of convergence rates of plots shown in Fig. 5. Convergence values are determined through a linear regression over numerical data from 5 to 50 grid nodes. Unless otherwise specifically stated, solutions take $\Lambda = \frac{1}{4}$. The MR slip schemes (not shown here) are exact for all slip-flow regimes, for all Λ values, and for all grid resolutions H; hence, concept of grid convergence does not apply.

	(a) No slip	(b) First-order slip	(c) Second-order slip
BB	−1.99	0.02	0.01
BB $\Lambda(C_1)$	−1.99	−1.99	0.07
BB $\Lambda(C_1,C_2)$	−1.99	−1.99	−1.99
CK	−1.99	−1.99	0.07
CK $\Lambda(C_2)$	−1.99	−1.99	−1.99
LI slip	−1.99	−0.93	−0.24
LI slip $\Lambda(C_1)$	−1.99	−1.99	0.07
LI slip $\Lambda(C_1,C_2)$	−1.99	−1.99	−1.99

Comment on the simulation of pressure-driven flows

As briefly pointed out in Remark 2 of Sec. IV, the CK schemes fail to maintain their accuracy for nonuniform pressure fields. Here, we prove this result by reassessing the previous case, now for a pressure-driven Poiseuille gas flow. For that, let us rewrite Eq. (25) considering a pressure gradient in bulk and the closure relation of CK schemes at boundaries [Eq. (17)]. As before, let us consider a horizontal channel ($\Theta = 1$) with halfway walls ($\delta_y = \frac{1}{2}$) so that the channel effective width is $H = N_y$. The formulation of the pressure-driven problem reads as follows:

$$-\partial_x P + \nu\rho_0\partial_y^2 u_x = 0 \quad \text{for} \quad y \in \left]-\frac{N_y}{2}+\frac{1}{2},\frac{N_y}{2}-\frac{1}{2}\right[, \tag{29a}$$

$$u_x \mp \left(\frac{1}{2}+C_1\lambda\right)\partial_y u_x + \left(\frac{2}{3}\Lambda+\frac{1}{2}C_1\lambda\right)\partial_y^2 u_x\big|_{y_b=\mp\frac{N_y}{2}\pm\frac{1}{2}} = \frac{C_1\lambda}{6\nu\rho_0}\partial_x P. \tag{29b}$$

The solution of Eq. (29a) subject to Eq. (29b) is given in normalized form as follows:

$$\begin{aligned} \tilde{u}_x &= 1-4\tilde{y}^2+4C_1\mathrm{Kn}-\epsilon\frac{4}{3}C_1\mathrm{Kn}+\epsilon^2\left(\frac{16}{3}\Lambda-1\right), \\ \tilde{y} &= \frac{y}{H} \in \left[-\frac{1}{2},\frac{1}{2}\right], \\ \tilde{u}_x &= \frac{u_x}{u_0}, \quad u_0 = -\frac{\partial_x P\, H^2}{8\nu\rho_0}, \quad \epsilon = \frac{1}{H}, \quad \mathrm{Kn} = \frac{\lambda}{H}. \end{aligned} \tag{30}$$

Comparing Eq. (30) with the exact solution $\tilde{u}_x^{(\mathrm{exact})}$ [Eq. (24)], we observe that the LBM solution introduces the following numerical slip:

$$\Delta\tilde{u}_x = \tilde{u}_x - \tilde{u}_x^{(\mathrm{exact})} = 8C_2\mathrm{Kn}^2 - \epsilon\tfrac{4}{3}C_1\mathrm{Kn}+\epsilon^2\left(\tfrac{16}{3}\Lambda-1\right). \tag{31}$$

We recall the numerical slip in the force-driven case reads as $\Delta\tilde{u}_x = 8C_2\mathrm{Kn}^2+\epsilon^2(\frac{16}{3}\Lambda-1)$, which is obtained by introducing the $\alpha^{\pm}$ coefficients for the CK scheme given in Table VIII into Eq. (27). The comparison of the two cases reveals the inferior accuracy of the pressure-driven solution since $\Delta\tilde{u}_x$ given by Eq. (31) is affected by a first-order error, i.e., the term proportional to ϵ. This numerical slip artificial can be vanished with the calibration $\Lambda = \frac{3}{16}(1+\frac{4}{3}C_1\lambda+8C_2\lambda^2)$, which differs from the equivalent force-driven Λ calibration $\Lambda = \frac{3}{16}(1+8C_2\lambda^2)$ (see Table IV). We note that, based on the analysis developed in Sec. IV, it is straightforward to extend this Λ-based calibration from $\delta_y = \frac{1}{2}$ to arbitrary $\delta_y \in [0,1]$.

The duality between pressure- and force-driven solutions above shown is absent from the LBM solutions obtained with the slip boundary schemes proposed in this paper (and also the BB rule). Given that incompressible flow solutions must hold invariant with the respect to the transformation $F_x \to -\partial_x P$, the conclusion is that CK schemes have an inconsistent behavior for incompressible hydrodynamics, a defect not reported in previous studies.

C. LBM velocity profile in lattice-inclined channel

For the study of the lattice-inclined channel it is more convenient to consider for reference analytical solution $j_q^{(\mathrm{exact})}$, which denotes the Poiseuille flow profile projected on the lattice space. Here, spatial variations are measured with respect to the link coordinate y_q, i.e., the projection of the rotated y' axis along the axis parallel to $\{\vec{c}_q,\vec{c}_{\bar{q}}\}$ [see Fig. 2(b)]. Once again, the flow is assumed steady and unidirectional $u_{x'}^{(\mathrm{exact})}$ and driven by a constant body force $F_{x'}$ (with no pressure gradient imposed); the walls are at rest ($U_w = 0$) and the fluid-wall interactions are assumed to be modeled by the second-order slip velocity condition. The lattice-projected Poiseuille flow analytical solution $j_q^{(\mathrm{exact})}$ reads as

$$\begin{aligned} j_q^{(\mathrm{exact})}(y_q) &= \frac{F_q}{8\nu}\left(H_q^2-4y_q^2+4C_1\lambda_q H_q+8C_2\lambda_q^2\right), \\ H_q &= \frac{H}{\Theta_q}, \quad \lambda_q = \frac{\lambda}{\Theta_q}, \\ &= \frac{F_q H_q^2}{8\nu}\left[1-4\left(\frac{y_q}{H_q}\right)^2+4C_1\mathrm{Kn}+8C_2\mathrm{Kn}^2\right], \\ \mathrm{Kn} &= \frac{\lambda_q}{H_q} = \frac{\lambda}{H}. \end{aligned} \tag{32}$$

The channel walls are located at $y_{qw} = \pm H_q/2$ or, equivalently, at $y_{qw} = \pm(y_{q\mathrm{b}}+\delta_q)$, if measuring the wall locations with respect to the boundary nodes $y_{q\mathrm{b}}$. Equation (32) reduces to the lattice-aligned horizontal channel solution [Eq. (24)] when $\Theta_q = \Theta = 1$, which reads for the nontrivial links $c_{qx}c_{qy} \neq 0$ as follows: $u_x^{(\mathrm{exact})}(y) = \frac{F_x}{8\nu\rho_0}(H^2-4y^2+4C_1\lambda H+8C_2\lambda^2)$.

In comparison to the lattice-aligned case, the new error source introduced by the inclined channel modeling is the discretization of the non-mesh-aligned walls. This error arises when the condition on the boundary is not sufficiently accurate to guarantee that the discrete walls match the real ones. The result is perceived by the numerical velocity profiles with the creation of *spurious accommodation layers* [67–69,97,123]. Such numerical boundary layers should be vanished,

TABLE X. Calibration of Λ for each slip boundary scheme considered in the study of the inclined channel flow. Note, these Λ values yield the exact slip velocity condition in the case of horizontal lattice-aligned channels, not for inclined channels. The BB and CK[$\frac{1}{2}$] scheme consider $\delta_y = \frac{1}{2}$, whereas the CK[δ_y] and LI slip schemes consider a free $\delta_y \in [0,1]$, where δ_y is the distance from the boundary node to the wall, measured along its normal direction, and with δ_y attributed to all wall cut links q. TRT model is considered herein (the conversion to other collision models follows from Table II).

	Λ
BB scheme [Eq. (20)]	$\frac{3}{2}(\frac{1}{8}+\frac{1}{2}C_1\lambda H + C_2\lambda^2)$
CK[$\frac{1}{2}$] scheme [Eq. (17) with Eq. (18)]	$\frac{3}{2}(\frac{1}{8}+C_2\lambda^2)$
CK[δ_y] scheme [Eq. (17) with Eq. (19)]	$\frac{3}{2}[\frac{1}{2}(\delta_y^2-\delta_y+\frac{1}{2})+C_1\lambda(\delta_y-\frac{1}{2})+C_2\lambda^2]$
LI slip scheme [Eq. (22)]	$\frac{3}{2}(\frac{\delta_y^2}{2}+C_1\lambda\delta_y+C_2\lambda^2)$
MR slip scheme [Eq. (13)]	$\forall\ \mathbb{R}^+$

particularly when physical Knudsen layers are to be considered, e.g., using effective viscosity approaches [14,39,41,50,54,62,86]. For that reason, we will pay particular attention to these artifacts in the analysis below. Without loss of generality, the simulations consider the inclined channel to make an angle $\theta = \tan^{-1}(\frac{1}{2})$ with the horizontal axis of the lattice [see Fig. 2(c)]. The slip walls are modeled with five different boundary schemes, namely, (i) BB, (ii) CK[$\frac{1}{2}$], (iii) CK[δ_y], (iv) LI slip, and (v) MR slip. The difference between the CK slip schemes (ii) and (iii) is that the former considers the standard CK algorithm, which is limited to $\delta_y = \frac{1}{2}$, e.g., [55], while the latter operates with an improved version where arbitrary $\delta_y \in [0,1]$ walls are considered, as explained in Remark 4 of Sec. IV (i.e., the slip boundary scheme for "curved walls" proposed in [56] further discussed in Appendix B). Regarding the Λ specification, since no Λ strategy is available to recover exact solutions in non-mesh-aligned boundaries, we adopt the Λ value that would otherwise produce the exact slip velocity condition in the horizontal lattice-aligned channel setup; these Λ calibrations are summarized in Table X. The effect of Λ on each of these boundary schemes will be discussed at the end of the section. We note that the choice of the collision model only effects the interpretation of the numerical results in the meaning of Λ (see Table II). In this context, we notice that collision operators with $\Lambda(\nu)$ violate the consistency requirement of viscosity-independent permeability for channel solutions [63,73,93,100,113,120,124]. Such a defect, originally identified for hydrodynamic solutions in the no-slip regime [63], is also present in the slip-flow regime, with error form being dependent on the LBM collision operator.

Figure 6 shows the velocity profiles $\tilde{u}_{x'}$ predicted by the LBM with each of the five families of slip boundary schemes. The parabolic accurate MR slip exactly captures the analytical solution [Eq. (32)], for all slip-flow regimes. On the other hand, all other slip schemes exhibit growing differences to the expected analytical profile as the order of the slip condition increases. Figures 7, 8, and 9 intend to illustrate such differences, revealing how bulk solutions become distorted when they are accommodated by inaccurate boundary conditions, in this less trivial simulation scenario of non-mesh-aligned walls. Next, we will discuss the impact of this issue on the quality of the predicted LBM profiles.

Figure 7 displays the error profiles of the streamwise component of fluid velocity $\Delta\tilde{u}_x$ along the channel width. In the no-slip regime, we notice that, together with an approximately uniform error at the channel center, there is a sharp variation of the error nearby the boundaries. This is a manifestation of the, previously mentioned, spurious accommodation layers, which should not be confused with physical Knudsen layers. While this latter has a physical origin, the former is created by numerical artifacts. In terms of global error, there is an order of magnitude loss of accuracy from LI slip to BB or kinetic LBM boundary schemes (cf. Table XI). When the no-slip wall regime evolves to a slip one, the form and magnitude of the error change. The most striking feature is the apparent diminishing in importance of the spurious accommodation layers as the slip-flow regime intensifies. This is confirmed by two features: (i) the absence of sharp variations in the error profile nearby the boundary and (ii) the almost uniform error throughout the channel full width, although the magnitude of this $\Delta\tilde{u}_x$ error increases considerably with the order of the slip condition (cf. Table XI). This result points to the superior impact of the order of accuracy of the slip boundary schemes on the quality of the velocity profiles in the slip-flow regime.

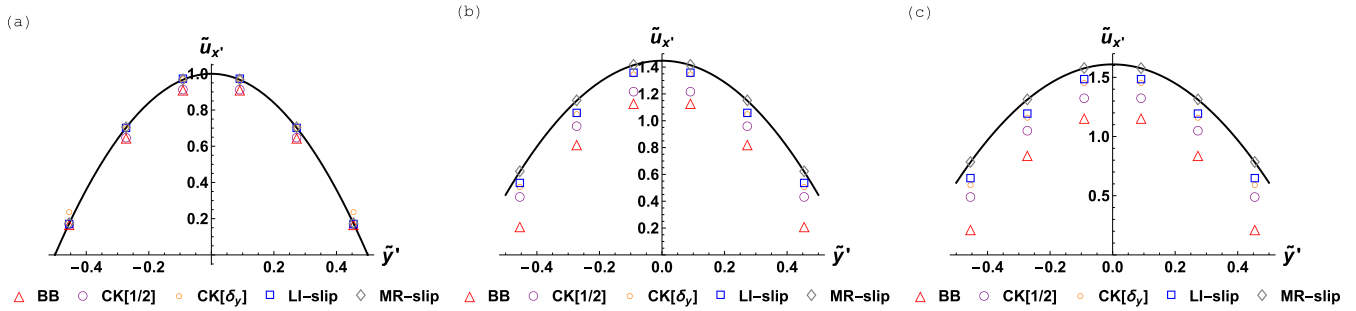

FIG. 6. Poiseuille flow velocity solutions at Kn = 0.1 within slip-flow theory. Continuous black line represents exact analytical solution [Eq. (32)]. Markers denote the LBM nodal point solutions, which are predicted by different slip boundary schemes. All cases refer to inclined channel [$\theta = \tan^{-1}(\frac{1}{2})$], resolved by $N_y = 6$ grid nodes along its width. (a) No-slip velocity boundary condition ($C_1 = C_2 = 0$). (b) First-order slip velocity boundary condition ($C_1 = 1.0$ and $C_2 = 0$ by Maxwell [15]). (c) Second-order slip velocity boundary condition ($C_1 = 1.1466$ and $C_2 = 0.9576$ by Cercignani [21]).

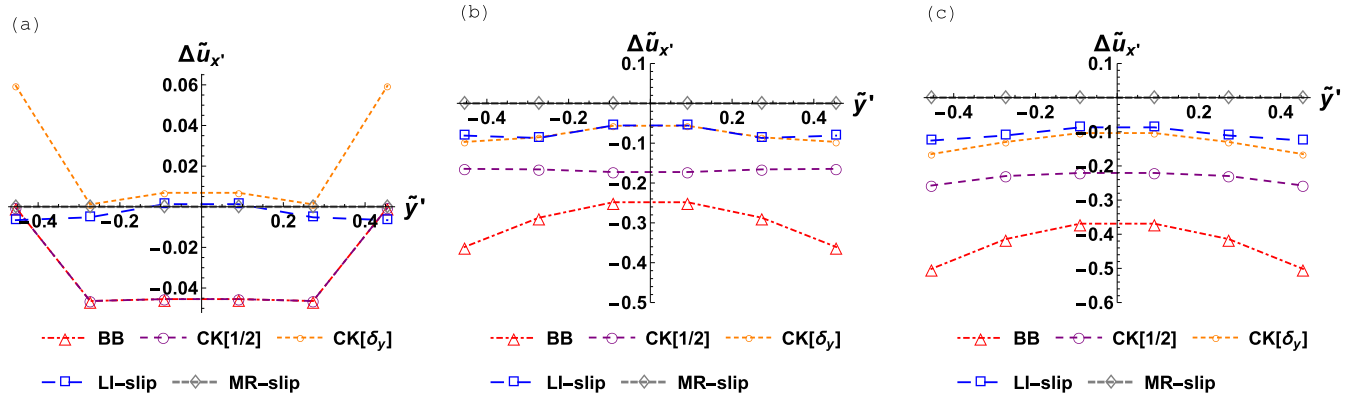

FIG. 7. Error profiles, from Fig. 6, of streamwise velocity component $\Delta\tilde{u}_{x'} = \tilde{u}_{x'} - \tilde{u}_{x'}^{(\mathrm{exact})}$, where $\tilde{u}_{x'} = j_q/j_q^{(\mathrm{max})}$ and the analytical solution $\tilde{u}_{x'}^{(\mathrm{exact})} = j_q^{(\mathrm{exact})}/j_q^{(\mathrm{max})}$, with $j_q^{(\mathrm{exact})}$ given by Eq. (32) and $j_q^{(\mathrm{max})} = F_q H_q^2/(8\nu)$. The mean error $\langle\Delta\tilde{u}_{x'}\rangle$ is quantified in Table XI. Panel (a): No-slip velocity boundary condition ($C_1 = C_2 = 0$). Panel (b): First-order slip velocity boundary condition ($C_1 = 1.0$ and $C_2 = 0$ by Maxwell [15]). Panel (c): Second-order slip velocity boundary condition ($C_1 = 1.1466$ and $C_2 = 0.9576$ by Cercignani [21]).

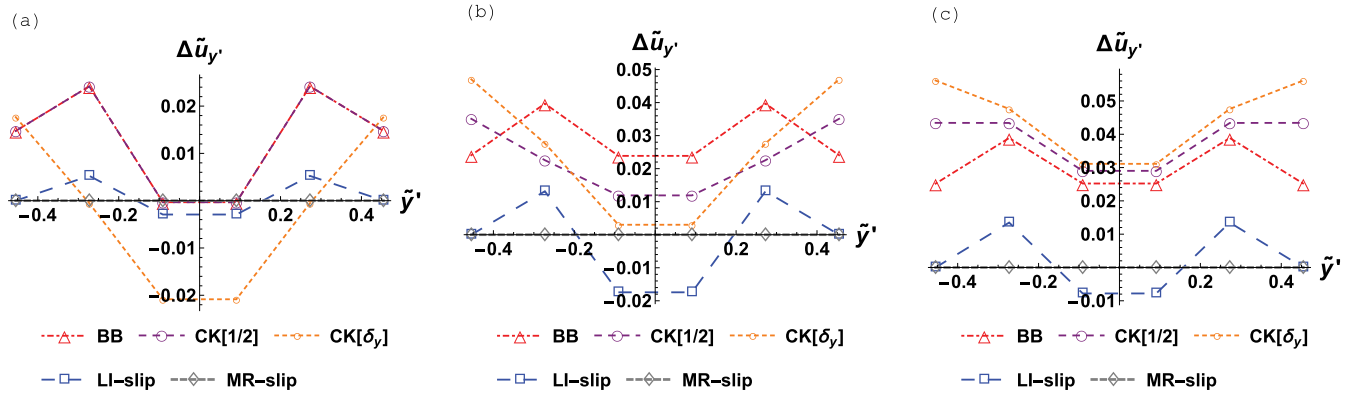

FIG. 8. Error profiles, from Fig. 6, of transversal velocity component $\Delta\tilde{u}_{y'} = \tilde{u}_{y'} - \tilde{u}_{y'}^{(\mathrm{exact})}$, where analytical solution is $\tilde{u}_{y'}^{(\mathrm{exact})} = 0$. The mean error $\langle\Delta\tilde{u}_{y'}\rangle$ is quantified in Table XI. Panel (a): No-slip velocity boundary condition ($C_1 = C_2 = 0$). Panel (b): First-order slip velocity boundary condition ($C_1 = 1.0$ and $C_2 = 0$ by Maxwell [15]). Panel (c): Second-order slip velocity boundary condition ($C_1 = 1.1466$ and $C_2 = 0.9576$ by Cercignani [21]).

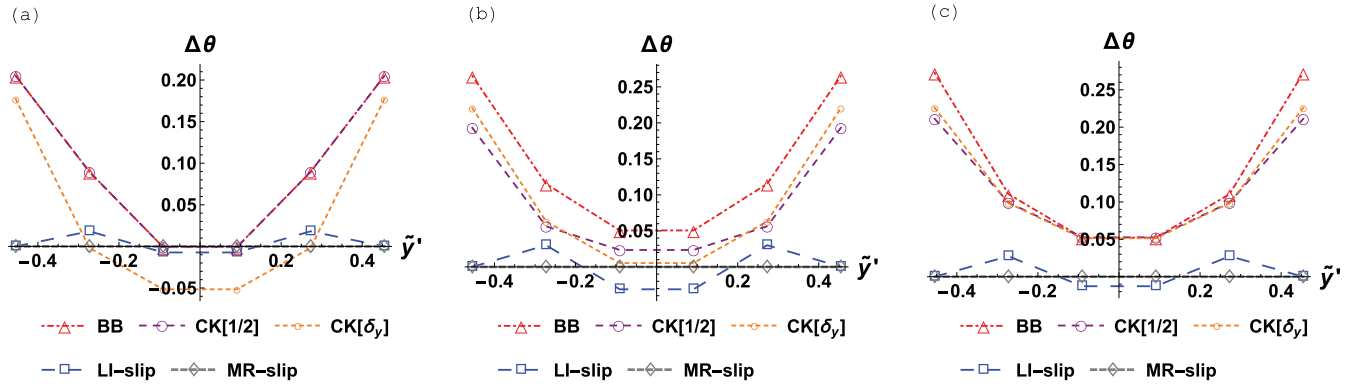

FIG. 9. Error profiles of flow streamlines angle $\theta = \tan^{-1}(\tilde{u}_y/\tilde{u}_x)$ (measured with respect to the fixed, lattice-aligned frame (x, y)) and determined as $\Delta\theta = \theta/\theta^{(\mathrm{exact})} - 1$, where analytical solution is given by $\theta^{(\mathrm{exact})} = \tan^{-1}(1/2)$. The mean error $\langle\Delta\theta\rangle$ is quantified in Table XI. Panel (a): No-slip velocity boundary condition ($C_1 = C_2 = 0$). Panel (b): First-order slip velocity boundary condition ($C_1 = 1.0$ and $C_2 = 0$ by Maxwell [15]). Panel (c): Second-order slip velocity boundary condition ($C_1 = 1.1466$ and $C_2 = 0.9576$ by Cercignani [21]).

TABLE XI. Error mean values $\langle \Delta\tilde{u}_{x'} \rangle = \frac{1}{N_y} \sum \Delta\tilde{u}_{x'}$, $\langle \Delta\tilde{u}_{y'} \rangle = \frac{1}{N_y} \sum \Delta\tilde{u}_{y'}$, and $\langle \Delta\theta \rangle = \frac{1}{N_y} \sum \Delta\theta$ for the error plots shown in Figs. 7, 8, and 9, respectively. Parabolic-slip solutions are exact, up to the roundoff error, for all tests shown in this table.

	(a) No slip	(b) First-order slip	(c) Second-order slip
		$\langle \Delta\tilde{u}_{x'} \rangle$	
BB	-0.031	-0.299	-0.428
CK[$\frac{1}{2}$]	-0.031	-0.168	-0.236
CK[δ_y]	0.023	-0.079	-0.133
LI slip	-0.003	-0.074	-0.108
		$\langle \Delta\tilde{u}_{y'} \rangle$	
BB	0.013	0.029	0.030
CK[$\frac{1}{2}$]	0.013	0.023	0.039
CK[δ_y]	-0.001	0.026	0.045
LI slip	7×10^{-4}	-0.001	0.002
		$\langle \Delta\theta \rangle$	
BB	0.098	0.143	0.145
CK[$\frac{1}{2}$]	0.098	0.091	0.121
CK[δ_y]	0.041	0.096	0.125
LI slip	0.004	-3×10^{-4}	0.005

Figure 8 displays the error profiles of the transversal component of fluid velocity $\Delta\tilde{u}_y$ along the channel width. Theoretically, the expected transversal velocity solution should be $\tilde{u}_{y'}^{(\text{exact})} = 0$. The fact that $\tilde{u}_{y'} \neq 0$ is indicative of wall discretization artifacts. More precisely, it is the attempt to accommodate the inclined Poiseuille flow solution on the low-order boundary conditions that generates the nonvanishing transverse velocity component. A proof is that in lattice-aligned channels $\tilde{u}_{y'} = 0$ is always recovered, irrespective of the accuracy order of the LBM boundary scheme considered. Other proof that $\tilde{u}_{y'} \neq 0$ is primarily generated by spurious accommodation layers lies in the structure of the error profiles: they have a uniform value at the channel center only notoriously varying nearby boundaries. This behavior holds for almost all LBM slip velocity schemes, and the error magnitude remains approximately unchanged with the slip order (cf. Table XI). The exception is the parabolic MR slip scheme which guarantees $\tilde{u}_{y'} = 0$, up to the roundoff error.

Figure 9 displays the profiles of the loss of rotational invariance in the velocity field. The angular deviations are quantified by $\Delta\theta$, which is defined within the caption of Fig. 9. The rotational invariance analysis basically confirms the study of $\tilde{u}_{y'}$, and both highlight the negative impact of the low-order boundary schemes as slip wall conditions. Because of their deficient accommodation of the bulk solution, they give rise to spurious accommodation layers, which distort the velocity field streamlines, deviating them from holding parallel to the channel inclination. Compared to BB and CK schemes, the LI slip shows a better performance in supporting the rotational invariance of the bulk solution (cf. Table XI). In all cases, the parabolic MR slip schemes exactly guarantee $\theta = \theta^{(\text{exact})}$.

Figure 10 shows the effect of Λ on the accuracy $|\mathcal{E}(\tilde{u}_{x'})|$, for fixed grid resolution. Before analyzing this case, it is important to recall the lattice-aligned one (with $\delta_y = \frac{1}{2}$) discussed in Fig. 4. In that case, most of boundary schemes (except BB) managed to cope with this problem correctly up to the first order in their coefficients. As such, the accuracy of these LBM solutions was essentially dominated by the Λ parameter at the second order. The inclined channel case, however, introduces the discretization of the boundary as a first-order artifact (manifested in the staircase wall approximation). Therefore, the Λ value that weighs second-order terms appears to have a reduced influence on the accuracy of solutions that fail to be correct, already, at the first order. This explains the less pronounced dependence of $|\mathcal{E}(\tilde{u}_{x'})|$ on Λ, and also why the exact solutions are never achieved (contrary to the lattice-aligned channel case). Given that Λ cannot be adjusted independently link per link (recall Remark 3 in Sec. IV), the best one can expect with the calibration of relaxation parameters is improvements of the order of magnitude of those shown in Fig. 10.

Figure 11 shows the effect of the grid resolution on the accuracy $|\mathcal{E}(\tilde{u}_{x'})|$, fixing Λ. That is, we still use Λ has given by Table X, but fixing $\delta_y = \frac{1}{2}$ in its calibration for all cases. In fact, numerical tests have suggested that, with a spatially varying calibration of the kind $\Lambda(\delta_y)$, solutions become more sensitive to numerical instabilities. For no-slip boundaries, the CK[$\frac{1}{2}$] reduces to the BB rule. The CK[δ_y] differs due to its extra degree of freedom, set by the $\sigma(\delta_y)$ calibration [Eq. (19)] (note that contrary to Λ we allow σ to vary with δ_y). These three cases indicate a first-order convergence with

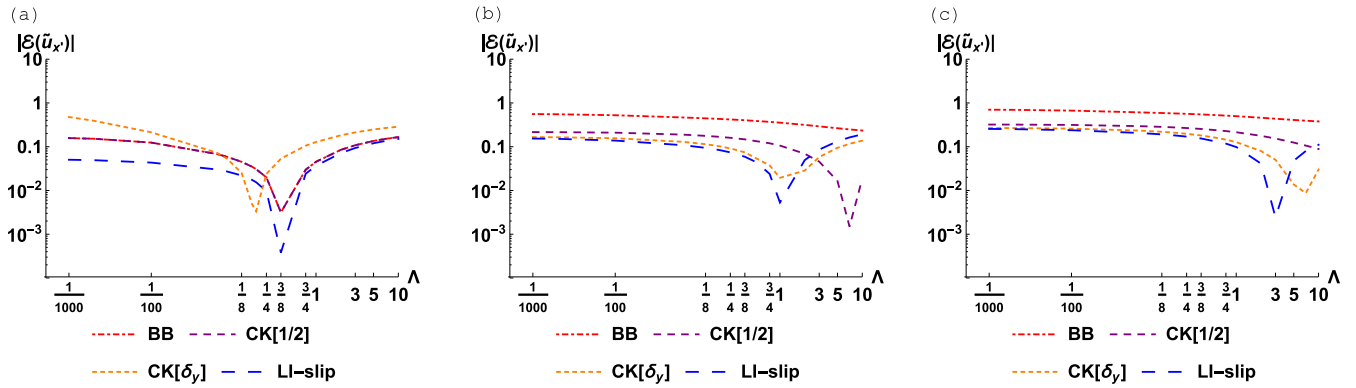

FIG. 10. Accuracy $|\mathcal{E}(\tilde{u}_{x'})|$ as function of relaxation parameter Λ. All cases refer to inclined channel [$\theta = \tan^{-1}(\frac{1}{2})$] resolved by $N_y = 6$ grid nodes its along width. (a) No-slip flow regime (Kn = 0). (b) First-order slip-flow regime (Kn = 0.1, $C_1 = 1$ [15]). (c) Second-order slip-flow regime (Kn = 0.1, $C_1 = 1.1466$, and $C_2 = 0.9576$ [21]). The MR slip schemes (not shown here) are exact for all slip-flow regimes and for all Λ values.

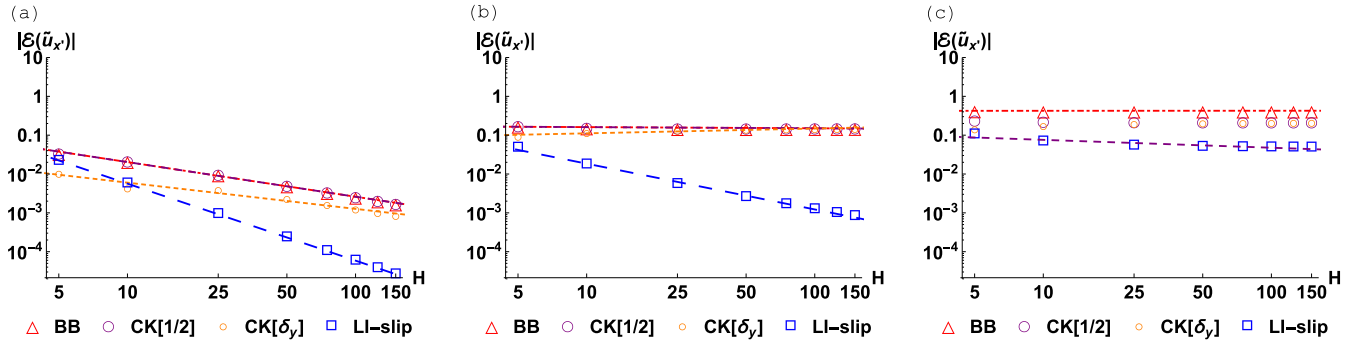

FIG. 11. Accuracy $|\mathcal{E}(\tilde{u}_x)|$ as function of grid resolution H, with Λ fixed and given by Table X, with $\delta_y = \frac{1}{2}$. Convergence rates are quantified in Table XII. (a) No-slip flow regime (Kn = 0). (b) First-order slip-flow regime (Kn = 0.1, $C_1 = 1$ [15]). (c) Second-order slip-flow regime (Kn = 0.1, $C_1 = 1.1466$, and $C_2 = 0.9576$ [21]). The MR slip schemes (not shown here) are exact for all slip-flow regimes, $\forall$ Λ values and $\forall$ H; hence, the concept of grid convergence does not apply.

grid resolution which is observed in Fig. 11(a) and quantified in Table XII. On the other hand, the LI slip schemes are formally second-order accurate in the no-slip limit, which is confirmed by the second-order convergence rate in Fig. 11(a) and Table XII. However, as expected, these convergence characteristics deteriorate significantly with the modeling of the first-order slip condition. Here, BB and CK schemes fail already to provide the correct first-order coefficient, which makes them formally zeroth-order accurate. That is, they do not converge with the grid-resolution refining [see Fig. 11(b)]. Such a result is the numerical proof of the *inconsistency* of kinetic LBM boundary schemes as numerical models for the first-order slip velocity condition (and obviously for the second-order slip condition, as discussed next). On the other hand, the LI slip schemes are correct in their first-order coefficients. However, as pointed out in the analysis of Fig. 5, with the exception of a very specific choice of Λ (generally not available in arbitrary geometries), the second-order coefficient of LI slip schemes preserves artifacts that are actually first order with the mesh spacing, and this explains the first-order convergence rate observed in Fig. 11(b) and in Table XII. The most disturbing findings appear in the modeling of the second-order slip condition. As shown in Fig. 11(c) and in Table XII, neither CK nor LI slip schemes converge with the grid resolution. This means that both schemes are *inconsistent* numerical models for the second-order slip velocity condition. Such a result is the numerical confirmation that the necessary condition for the *consistent modeling of the slip-flow regime* (both at first and second order) implies the parabolic accuracy of LBM boundary schemes. Indeed, for general plane wall configurations, where the "absorption" of numerical errors into physical slip through calibration is not available, the fulfillment of this condition is only possible by using slip schemes that support the parabolic accuracy by design, which is the case of the MR slip schemes presented in Sec. VI.

TABLE XII. Quantification of convergence rates, which are obtained through a linear regression over numerical data, of the convergence plots shown in Fig. 11. The MR slip schemes (not shown here) are exact for all slip-flow regimes, $\forall$ Λ values and $\forall$ H, meaning the concept of grid convergence does not apply.

	(a) No slip	(b) First-order slip	(c) Second-order slip
BB	−0.893	−0.030	−0.002
CK[$\frac{1}{2}$]	−0.893	−0.030	−0.026
CK[δ_y]	−0.676	0.124	0.102
LI slip	−1.982	−1.179	−0.203

VIII. BENCHMARK RESULTS: KNUDSEN'S PARADOX

As commented in the introduction of Sec. VII, the ability of LBM boundary schemes to support the slip velocity condition can be also evaluated on the basis of the dependence of the normalized mass flow rate $\widetilde{Q}$ with Kn. This problem gives rise to the well-known Knudsen's paradox, which states the existence of a minimum in the $\widetilde{Q}$(Kn) evolution [2–5,12,13]. Such a benchmark test has been used by a number of LBM studies; a far from exhaustive list is [39,41,44,54,61,62,83,87,88,90,106–108]. While in theory the Knudsen's paradox is equivalent to the study reported in Sec. VII, concerning the direct measurement of the wall slip in the velocity profile, the LBM predictions in this last case may not lead to identical conclusions due to the interference of numerical integration errors. The first part of this section addresses this issue. The second part focuses on the impact of different slippage coefficients, e.g., as those given in Table I, over the performance of the LBM slip boundary schemes.

A. Analytical Knudsen's minimum

Let us assume the normalized Poiseuille flow solution given by $\tilde{u}_x^{(\text{exact})}$ in Eq. (24). Then, the *exact* computation of the normalized mass flow rate on the *exact* profile yields [12–14]

$$\widetilde{Q}^{(\text{exact})} = \frac{1}{4\,\text{Kn}} \int_{-1/2}^{1/2} \tilde{u}_x^{(\text{exact})}(\tilde{y})\, d\tilde{y} = \frac{1}{6\,\text{Kn}} + C_1 + 2C_2\text{Kn}. \tag{33}$$

Figure 12 plots the solution of Eq. (33) for the four slip-flow conditions: (i) no slip ($C_1 = C_2 = 0$), (ii) first-order slip ($C_1 = 1.0$ and $C_2 = 0$ by Maxwell [15]), (iii) second-order slip ($C_1 = 1.1466$ and $C_2 = 0.9576$ by Cercignani [21]), and (iv) second-order slip [C_1(Kn) and C_2(Kn) by Wang *et al.* [20]]. The curves associated with the second-order slip velocity models clearly exhibit a minimum, which is

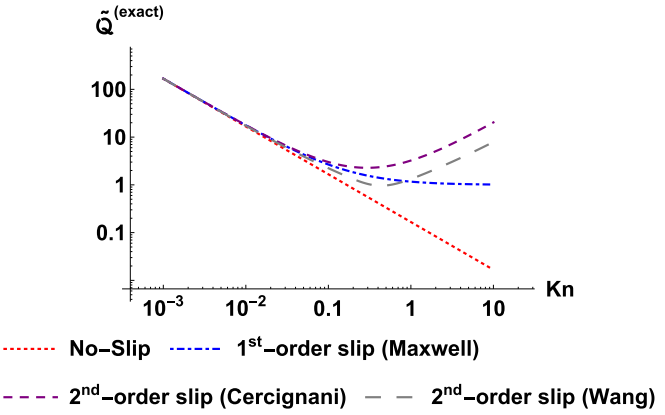

FIG. 12. Normalized mass flow rate [Eq. (33)] as function of Kn for the three slip-flow conditions: (i) no slip ($C_1 = C_2 = 0$), (ii) first-order slip ($C_1 = 1.0$ and $C_2 = 0$ by Maxwell [15]), (iii) second-order slip ($C_1 = 1.1466$ and $C_2 = 0.9576$ by Cercignani [21]), and (iv) second-order slip [C_1(Kn) and C_2(Kn) as in Table I by Wang *et al.* [20]].

known as *Knudsen's minimum*. Theoretically, this mass flow rate minimum is found by computing the positive root of $\partial \widetilde{Q}^{(\text{exact})}/\partial \,\text{Kn} = 0$. When the C_1 and C_2 coefficients are Kn independent, the Knudsen's minimum $\text{Kn}|_{\text{min}}^{(\text{exact})}$ is explicitly given by [2,12–14]

$$\text{Kn}|_{\text{min}}^{(\text{exact})} = \frac{1}{2\sqrt{3\,C_2}}. \tag{34}$$

For example, in the Cercignani model [21], Eq. (34) predicts $\text{Kn}|_{\text{min}}^{(\text{exact})} \simeq 0.3$. When C_1 and C_2 are functions of Kn, such as in [19,20], then $\text{Kn}|_{\text{min}}^{(\text{exact})}$ may not be available explicitly. For example, in the Wang *et al.* model [20] we have determined $\text{Kn}|_{\text{min}}^{(\text{exact})} \simeq 0.4$, using the built-in root finder of *Mathematica*.

B. LBM Knudsen's minimum in lattice-aligned horizontal channel: Effect of integration scheme

For illustrative purposes let us focus on the most favorable case of Poiseuille flow in a lattice-aligned horizontal channel with midway walls $\delta_y = \frac{1}{2}$. Here, LBM exact solutions are available, which are given by Eq. (25) with coefficients given in Table VIII. The key point in the Knudsen's minimum analysis is the computation of mass flow rate. While this step requires the evaluation of an integral [Eq. (33)], in simulations a numerical quadrature must be adopted. Often, *low-order quadrature* methods are used, such as the midpoint rule, where the nodal solutions are subject to simple summations [125]. In this case, the computation of the mass flow rate $\widetilde{Q}^{(\text{num})}$ through summation yields the following prediction:

$$\widetilde{Q}^{(\text{num})} = \frac{1}{4\,\text{Kn}}\sum_j \tilde{u}_x(\tilde{y}_j) = \frac{1}{6\,\text{Kn}} + \frac{\epsilon}{\text{Kn}}\left(\alpha^+ - \frac{1}{2}\right) + \frac{\epsilon^2}{3\,\text{Kn}}(1 - 3\alpha^+ + 6\alpha^-). \tag{35}$$

Note that in deriving Eq. (35) the summation was performed over the nodal points $\tilde{y}_j = \frac{y_j}{H}$ with $y_j = -\frac{N_y}{2} + \frac{1}{2} + j$ and $j = 0,1,\ldots,N_y - 1$. For this task the computation of $\widetilde{Q}^{(\text{num})}$ employed $\tilde{u}_x$, as given by Eq. (25), and the $\alpha^{\pm}$ coefficients summarized in Table VIII. Table XIII lists the $\widetilde{Q}^{(\text{num})}$ solutions predicted by each slip boundary scheme.

TABLE XIII. Solutions of $\widetilde{Q}^{(\text{num})}$ obtained by substituting into Eq. (35) the explicit content of the $\alpha^{\pm}$ coefficients for each slip boundary scheme (cf. Table VIII).

	$\widetilde{Q}^{(\text{num})}$
BB	$\frac{1}{6\,\text{Kn}} + \frac{\epsilon^2}{6\,\text{Kn}}(8\Lambda - 1)$
CK[$\frac{1}{2}$]	$\frac{1}{6\,\text{Kn}} + C_1 + \frac{\epsilon^2}{6\,\text{Kn}}(8\Lambda - 1)$
LI slip	$\frac{1}{6\,\text{Kn}} + C_1 - \epsilon\,C_1 + \frac{\epsilon^2}{6\,\text{Kn}}(8\Lambda - 1)$
MR slip	$\frac{1}{6\,\text{Kn}} + C_1 + 2C_2\text{Kn} + \frac{\epsilon^2}{12\,\text{Kn}}$

In order to evaluate the accuracy of each boundary scheme, let us introduce the error measure

$$|\mathcal{E}(\widetilde{Q})| = \left|\frac{\widetilde{Q}^{(\text{num})} - \widetilde{Q}^{(\text{exact})}}{\widetilde{Q}^{(\text{exact})}}\right|, \tag{36}$$

where $\widetilde{Q}^{(\text{num})}$ is collected in Table XIII and $\widetilde{Q}^{(\text{exact})}$ is given by Eq. (33). Next, let us discuss each slip-flow condition individually.

The zeroth-order (no-slip) condition implies $C_1 = C_2 = 0$, which leads to $\widetilde{Q}^{(\text{exact})} = \frac{1}{6\,\text{Kn}}$. All boundary schemes agree with this solution up to second-order accuracy, i.e., $|\mathcal{E}(\widetilde{Q})| \propto \epsilon^2$. The low-order boundary schemes, as carrying a Λ dependency, can use this free parameter to cancel the second-order error and match the exact solution. The $|\mathcal{E}(\widetilde{Q})| = 0$ happens with $\Lambda = \frac{1}{8}$. We note the difference between the optimal Λ value in the mass flow rate compared to that of the exact parabolic profile, i.e., $\Lambda = \frac{3}{16}$. This difference is due to addition of the integration errors [94,125].

The first-order slip condition implies $C_1 \neq 0$ and $C_2 = 0$ which leads to $\widetilde{Q}^{(\text{exact})} = \frac{1}{6\,\text{Kn}} + C_1$. The BB prediction is generally zeroth-order accurate with respect to $\widetilde{Q}^{(\text{exact})}$, except when $\Lambda = \frac{1}{8} + \frac{3}{4}C_1\Lambda H$ (i.e., using a resolution-dependent Λ calibration), which leads to $|\mathcal{E}(\widetilde{Q})| = 0$. The LI slip predicts a first-order accurate solution, except when $\Lambda = \frac{1}{8} + \frac{3}{4}C_1\Lambda$, which ensures $|\mathcal{E}(\widetilde{Q})| = 0$. The CK and MR slip schemes are second-order accurate with respect to the exact solution. Yet, the former offers the possibility to have $|\mathcal{E}(\widetilde{Q})| = 0$ by setting $\Lambda = \frac{1}{8}$.

The second-order slip condition implies $C_1 \neq 0$ and $C_2 \neq 0$ which leads to $\widetilde{Q}^{(\text{exact})} = \frac{1}{6\,\text{Kn}} + C_1 + 2C_2\text{Kn}$ as in Eq. (33). Aside from the MR slip scheme, which maintains its second-order accuracy, all low-order boundary schemes become zeroth-order accurate. Table XIV summarizes the specific Λ calibrations that make $\widetilde{Q}^{(\text{num})} = \widetilde{Q}^{(\text{exact})}$ in each scheme. Table XIV also evidences the differences between the optimal Λ calibrations for the velocity and the mass flow rate solutions. We note the above results apply for any C_1 and C_2 values, regardless they are constant or Kn dependent, as those presented in Table I.

Finally, it is worthwhile commenting on the aggravated consequences of the integration error on the numerical computation of the Knudsen's paradox problem. Let us assume we

TABLE XIV. Differences between Λ calibrations using low-order LBM boundary schemes in modeling horizontal Poiseuille channel flow. $\Lambda(\tilde{u}_x^{(\mathrm{num})} = \tilde{u}_x^{(\mathrm{exact})})$ are calibrations for the exact velocity profile. $\Lambda(\widetilde{Q}^{(\mathrm{num})} = \widetilde{Q}^{(\mathrm{exact})})$ are calibrations for the exact mass flow rate. TRT model is considered herein (the conversion to other collision models follows from Table II).

	$\Lambda(\tilde{u}_x^{(\mathrm{num})} = \tilde{u}_x^{(\mathrm{exact})})$	$\Lambda(\widetilde{Q}^{(\mathrm{num})} = \widetilde{Q}^{(\mathrm{exact})})$
BB	$\frac{3}{16} + \frac{3}{4}C_1\lambda H + \frac{3}{2}C_2\lambda^2$	$\frac{1}{8} + \frac{3}{4}C_1\lambda H + \frac{3}{2}C_2\lambda^2$
CK[$\frac{1}{2}$]	$\frac{3}{16} + \frac{3}{2}C_2\lambda^2$	$\frac{1}{8} + \frac{3}{2}C_2\lambda^2$
LI slip	$\frac{3}{16} + \frac{3}{4}C_1\lambda + \frac{3}{2}C_2\lambda^2$	$\frac{1}{8} + \frac{3}{4}C_1\lambda + \frac{3}{2}C_2\lambda^2$

are operating with a slip boundary scheme that provides the exact velocity solution, e.g., the MR slip schemes presented in Sec. VI. It turns out that, even with an exact velocity profile, the use of a low-order integration scheme at the post-processing step inevitably introduces a second-order error in the mass flow rate computation. Worse, the subsequent determination of the Knudsen's minimum based on this estimate further degrades the accuracy of the post-processing outcome to first order. The proof behind this loss of accuracy can be analytically determined by computing $\partial\widetilde{Q}^{(\mathrm{num})}/\partial\,\mathrm{Kn} = -\frac{1}{6\,\mathrm{Kn}^2}(1+\frac{\epsilon^2}{2}) + 2C_2 = 0$, which yields $\mathrm{Kn}|_{\mathrm{min}}^{(\mathrm{num})} = \frac{1}{2}\sqrt{\frac{1+\epsilon^2}{3C_2}}$. That is, the equivalence between exact and numerical Knudsen's minima differs through a first-order error in mesh spacing: $\mathrm{Kn}|_{\mathrm{min}}^{(\mathrm{num})} \simeq \mathrm{Kn}|_{\mathrm{min}}^{(\mathrm{exact})} + \mathcal{O}(\epsilon)$. In conclusion, the numerical study of the Knudsen's paradox problem shall pay particular attention to numerical integration errors in the post-processing step, meaning higher-order quadrature schemes shall be adopted, with Simpson's rule recommended. Otherwise, efforts to accurately predict the velocity solution may become severally damaged by post-processing errors.

C. LBM Knudsen's minimum in lattice-aligned horizontal channel: Effect of slippage coefficients

Finally, this section evaluates the effect that slippage coefficients may have on the accuracy of the LBM slip boundary schemes. For this task, we keep focus on the Knudsen's minimum problem. However, now we compute $\widetilde{Q}^{(\mathrm{num})}$ with Simpson's rule, meaning integration errors are absent and the only error source comes from the LBM slip schemes. That is, our study will work out on the outcome provided by the exact integration of the numerical velocity profile $\tilde{u}_x$ [Eq. (26)], with $\delta_y = \frac{1}{2}$. The (normalized) mass flux is given by

$$\widetilde{Q}^{(\mathrm{num})} = \frac{1}{4\,\mathrm{Kn}}\int_{-1/2}^{1/2}\tilde{u}_x(\tilde{y})\,d\tilde{y} = \frac{1}{6\,\mathrm{Kn}} + \frac{\epsilon}{\mathrm{Kn}}\left(\alpha^+ - \frac{1}{2}\right) + \frac{\epsilon^2}{4\,\mathrm{Kn}}(1 - 4\alpha^+ + 8\alpha^-). \quad (37)$$

Table VIII contains the specific content of the $\alpha^{\pm}$ coefficients for the slip boundary schemes considered. Their substitution into Eq. (37) leads to the $\widetilde{Q}^{(\mathrm{num})}$ predictions summarized in Table XV. To understand how the accuracy of LBM predictions may be impacted by the choice of the slippage coefficients, we repeat the $|\mathcal{E}(\widetilde{Q})|$ error analysis given by Eq. (36). We

TABLE XV. Solutions of $\widetilde{Q}^{(\mathrm{num})}$ obtained by substituting into Eq. (37) the explicit content of the $\alpha^{\pm}$ coefficients for each slip boundary scheme (cf. Table VIII).

	$\widetilde{Q}^{(\mathrm{num})}$
BB	$\frac{1}{6\,\mathrm{Kn}} + \frac{\epsilon^2}{4\,\mathrm{Kn}}(\frac{16}{3}\Lambda - 1)$
CK[$\frac{1}{2}$]	$\frac{1}{6\,\mathrm{Kn}} + C_1 + \frac{\epsilon^2}{4\,\mathrm{Kn}}(\frac{16}{3}\Lambda - 1)$
LI slip	$\frac{1}{6\,\mathrm{Kn}} + C_1 - \epsilon\,C_1 + \frac{\epsilon^2}{4\,\mathrm{Kn}}(\frac{16}{3}\Lambda - 1)$
MR slip	$\frac{1}{6\,\mathrm{Kn}} + C_1 + 2C_2\mathrm{Kn}$

find that conclusions are similar to those observed in the numerical study of the velocity profile in horizontal channel, reported in Sec. VII B. As a conclusion, this study confirms that the MR slip schemes due to their superior accuracy are the only ones to exactly support the second-order slip velocity condition independently of C_1 and C_2 values, i.e., with either constant or Kn-dependent slippage coefficients. On the other hand, the low-order slip schemes do require Λ to be adjusted according to the intended C_1 and C_2 values, which may not be straightforward to apply, particularly when the slippage coefficients feature an intricate functional Kn dependence, e.g., Wu [19] or Wang *et al.* [20] models shown in Table I. This ability to support arbitrary slippage coefficients places the LBM as a consistent numerical solver for the slip-flow regime, meaning its applicability can be extended over arbitrary classes of rarefied gas problems simply by adjusting the slippage coefficients in the slip boundary conditions. For that purpose, only physical considerations need to be invoked, which is in contrast with the current practice adopted in LBM, where the popular kinetic-based slip schemes, as producing incorrect coefficients, must be subject to specific *ad hoc* numerical calibrations afterwards. Unfortunately, these numerical calibrations do not only lack physical support as they display a limited range of applicability as illustrated in this work.

IX. CONCLUSIONS

This work concerns the application of the lattice Boltzmann method (LBM) to the numerical simulation of low-speed and isothermal flows pertaining to the slip-flow regime. This physical framework concedes the classical hydrodynamic theory to hold valid in bulk, while at solid walls the no-slip velocity boundary condition shall be replaced by a slip one. In this context, Knudsen boundary layers take a vanishingly small portion of the fluid domain. Thereby, the slip-flow regime permits the study of the isolated effect of the fluid-wall interactions in LBM simulations.

Based on these considerations, our study focuses on the *consistent* formulation of boundary schemes for the LBM, which model the slip velocity condition. The justification to consider the LBM in this task does not come from its kinetic origin (unlike most previous attempts as reported in Sec. I). Rather, it is the fact that the typical LBM linkwise boundary schemes follow a closure relation with a structure similar to that of slip-flow theory: both cases are described by a truncated Taylor series of the fluid velocity at the boundary. This similarity makes the LBM a natural candidate to numerically

solve the slip-flow regime, particularly when compared to the more well-established CFD techniques. Another advantage of the LBM framework is the possibility to reach higher Kn number flow regimes, through higher-order LB formulations. While not explored in this work, the extension of the present results to such cases is programmed for future studies.

The key contribution of this work was the derivation of the LBM boundary closure relation that prescribes the second-order slip velocity condition on arbitrary wall discretizations, within the LBM uniform Cartesian mesh formulation. The necessary requirement to support this physical condition was shown to be the parabolic accuracy of the LBM boundary scheme, and we derived the explicit linkwise form of first- and second-order coefficients for slip velocity schemes. Based on this result, we critically evaluated the closure relations of existing kinetic-based LBM boundary schemes, and identified the following number of defects: (i) they may hold viscosity-dependent artifacts; (ii) they are inconsistent for nonuniform pressure fields, such as pressure-driven flows; (iii) they are anisotropic, meaning that a different condition holds as function of the wall-lattice orientation; (iv) they are low-order accurate, thus introducing discrete lattice effects in the coefficients of the boundary condition, which will perturb the physical slip value; and (v) they are inappropriate for arbitrary geometries since the calibration typically used in lattice-aligned setups, consisting of absorbing the numerical errors into the physical slip condition, is unavailable for arbitrary flows and/or wall-lattice orientations.

Upon recognizing the limitations plaguing the LBM performance of existing kinetic-based boundary schemes, we propose tackling this problem directly at the LBM discrete level. For this purpose, we used the multireflection framework and extended it to handle the slip velocity boundary condition. Here, we considered both linear (LI slip) and parabolic slip (MR slip) schemes. Each case presents a compromise between complexity and level of accuracy. LI slip schemes correct some defects of kinetic-based LBM schemes, while retaining the local implementation; however, they preserve accuracy limitations in arbitrary wall configurations. On the other hand, MR slip schemes, although slightly more complex to implement (as operating on a two-node update rule), support the necessary condition to consistently model the slip-flow regime in general flow configurations.

The performance of the above-mentioned LBM boundary schemes as slip velocity models was verified for the steady Poiseuille flow problem in the slip-flow regime. Particular attention was given to the quality of the velocity profiles, with focus on two issues: (i) the effective slip velocity at the wall and (ii) the deformation of the profile due to spurious accommodation layers. The numerical experiments considered two cases of wall discretization, namely, lattice-aligned and lattice-inclined walls. The Knudsen's paradox problem was also studied as a complementary benchmark test. The ensemble of numerical tests confirmed the superior accuracy of the schemes proposed in this work, revealing the clear superiority of the parabolically accurate MR slip schemes. Although only 2D problems were tested, we remark that the theory here presented applies equally to 3D domains. Moreover, while only planar walls were considered, in an upcoming publication we will address the issue of prescribing the velocity slip on curved solid boundaries, a case that must account for the surface curvature. Also, even though we have limited our study to the low-speed Stokes regime, we stress that the schemes here proposed are equally applicable to nonlinear Navier-Stokes flows; in this context, we refer to Appendix B of [93] for a summary on the expected complexities arising from the discretization of the nonlinear term. Finally, we note that in terms of numerical implementation, while developed in the frame of the TRT collision operator (and its subclasses like REG/S-REG or BGK), the LBM boundary schemes constructed and analyzed in this work can be directly extended to multiple relaxation time (MRT) models. In that regard, we suggest the straightforward application of the reasoning put forward in [94].

ACKNOWLEDGMENTS

The authors are deeply thankful to I. Ginzburg for her critical reading and the numerous comments and suggestions that helped improve the manuscript clarity. G. Silva acknowledges the financial support given by Fundação para a Ciência e Tecnologia through the Grant No. SFRH/BPD/111228/2015.

APPENDIX A: MRT, REG, AND BGK COLLISION MODELS IN LBM

This Appendix briefly revises the most relevant aspects of alternative LBM collision operators and their relation to the TRT collision model.

MRT: The most general collision operator in LBM is the multiple relaxation time (MRT) model [37,70,72,75,94]. Rather than operating on the populations f_q, the MRT operates on the moments m_k with $k = 1, \ldots, Q$. These moments are determined by the projections of f_q on the eigenvectors M_{kq} of the collision operator as follows: $m_k = M_{kq} f_q$ (where summation is implied over repeated indexes). The collision eigenvectors M_{kq} are formed by a complete and orthogonal set of discrete velocity polynomials, whose structure may be determined through different theoretical frameworks; examples are found in [37,63,72,75,94,126]. The associated eigenvalues s_k, which follow from this spectral decomposition, are related to the relaxation rates of the collision process. This decoupling of the collision eigenmodes permits their relaxation in an individual and independent manner, which is the principal asset of MRT.

A particularly interesting MRT formulation is the computationally efficient "symmetrized" MRT framework [94,126]. This idea explores the symmetry properties of the underlying lattice space, thus decomposing the original MRT vector space into $\mathrm{MRT}^{(+)}$ and $\mathrm{MRT}^{(-)}$ bases. As each of these groups operates on halved basis vectors, this permits reducing the number of collision operations to approximately half [94,126]. This symmetrized framework also facilitates the theoretical analysis of the MRT. Indeed, if representing $s_k = s_i^+ \cup s_j^-$, where $i = 1, \ldots, Q_m/2$ and $j = d+1, \ldots, Q_m/2$, it can be proven [73] that the impact of these collision eigenvalues on the macroscopic equations (at any order) is only perceptible through the associated eigenfunctions $\Lambda_i^+ = (\frac{1}{s_i^+} - \frac{1}{2})$ and $\Lambda_j^- = (\frac{1}{s_j^-} - \frac{1}{2})$. Most importantly, the steady-state mass and momentum conservation equations reproduced by the MRT-LBM

can be shown to be controlled in their truncations (i.e., beyond second order) exclusively by the free tunable (positive) parameters $\Lambda_{i,j} = \Lambda_i^+ \Lambda_j^-$.

For example, in the $d2Q9$ model, the following nine linearly independent moments can be constructed: $m_k = (\rho, \epsilon, \varepsilon, p_{xx}, p_{xy}, j_x, j_y, q_x, q_y)^\top$, where ρ is the density, ϵ is the energy, ε is the square of the energy, p_{xx} and p_{xy} are the diagonal and off-diagonal components of the viscous stress tensor, j_x and j_y correspond to the x and y components of momentum, and q_x and q_y relate to the x and y components of energy flux. Note, the elements in m_k are ordered in such a way that the first five belong to MRT$^{(+)}$ and the remaining four to MRT$^{(-)}$. On this basis, the corresponding relaxation rates are $s_k = (0, s_\epsilon^+, s_\varepsilon^+, s_\nu^+, s_\nu^+, 0, 0, s_q^-, s_q^-)^\top$. Thus, from the above exposed, the MRT steady-state solutions get controlled by the following three combinations [94]:

$$\Lambda_{j,k} = \Lambda_j^+ \Lambda_k^- = \{\Lambda_\nu^+ \Lambda_q^-, \Lambda_\epsilon^+ \Lambda_q^-, \Lambda_\varepsilon^+ \Lambda_q^-\}. \tag{A1}$$

To the best of our knowledge, the cast of MRT studies simulating the slip-flow regime, e.g., [50,51,55,56,62,80], agrees on the following conclusion: the major role in the accuracy of MRT solutions is played by $\Lambda_\nu^+ \Lambda_q^-$, whereas the other free tunable relaxation combinations $\Lambda_\epsilon^+ \Lambda_q^-$ and $\Lambda_\varepsilon^+ \Lambda_q^-$ have negligible impact. Based on this conclusion, we may adopt the simplification $\Lambda_\nu^+ = \Lambda_\epsilon^+ = \Lambda_\varepsilon^+ = \Lambda^+$ and $\Lambda_q^- = \Lambda^-$, so that MRT effectively reduces to TRT with the only control parameter available being $\Lambda = \Lambda^+ \Lambda^-$, which is sufficient for this class of problems in terms of accuracy control.

REG: The regularized (REG) collision operator [81,82,92] was originally developed independently from the MRT framework [70,72,75,94]. However, it is now recognized that the former can be considered as a subclass of the latter. The relationship between MRT and REG is natural in weighted orthogonal eigenvectors, where the two become equivalent under a specific relaxation setting [94,100,127,128], which will be discussed next. The reason for still considering REG separably from MRT is that REG is often credited as "the necessary collision model to correctly reproduce nonequilibrium flows," e.g., [80,82–87]. With this discussion our intent is to clarify how REG operates in the LBM algorithm. Although our analysis applies to standard lattices, e.g., $d2Q9$, where only Navier-Stokes order effects are preserved, its extension to higher-order lattices, e.g., [40–44], proceeds along the same lines.

The main premise of REG is the "filtering out" of the nonequilibrium contributions associated to moments beyond hydrodynamic level, the so-called ghosts [36,127]. They can be identified by formally writing the LBM populations as [127] $f_q = f_q^H + f_q^T + f_q^G$, where f_q^H, f_q^T, f_q^G refer to hydrodynamic, transport, and ghost modes. Taking for concreteness the $d2Q9$ model, each of these groups incorporates the following MRT moments: $f_q^H = \{\rho, j_x, j_y\}$, $f_q^T = \{\epsilon, p_{xx}, p_{xy}\}$, and $f_q^G = \{\varepsilon, q_x, q_y\}$. Notice REG operates with a nontraceless strain rate [127,128]. Thus, the ϵ mode, which controls bulk viscosity, falls into the transport mode category. As such, in REG all moments belonging to f_q^T share the same relaxation rate: $s_\epsilon^+ = s_\nu^+ = 1/\tau$ (related to fluid viscosity). The filtering out of f_q^G is set by the ghost relaxation rates: $s_\varepsilon^+ = s_q^- = 1$. By placing these results into Eq. (A1), one concludes that the REG steady-state solutions get controlled by the single relaxation combination

$$\Lambda = \tfrac{1}{2}\Lambda_\nu^+ = \tfrac{1}{2}\Lambda_\epsilon^+ = \tfrac{3}{2}\nu. \tag{A2}$$

The other independent relaxation combination in REG is restricted to the fixed value: $\Lambda_\varepsilon^+ \Lambda_q^- = \frac{1}{4}$. Equation (A2) implies that truncation errors in REG display a viscosity-dependent structure, like in BGK [73]. This is no surprise since both collision schemes depend on a single relaxation parameter. However, the two differ on how such a viscosity dependence scales within the spatial truncation errors: BGK scales $\propto \nu^2$ [73], while REG scales $\propto \nu$. Roughly speaking, this is the principal asset of REG over BGK for steady-state solutions. A more detailed discussion on this topic, also supported by results showing the exact structure of the truncation corrections of the REG scheme, will be addressed in a separate publication.

In the context of this work, we note that REG can be partially reproduced by TRT. We recall that TRT sets $\Lambda_\nu^+ = \Lambda_\epsilon^+ = \Lambda_\varepsilon^+ = \Lambda^+$ and $\Lambda_q^- = \Lambda^-$. Hence, if choosing $\Lambda^+ = 3\nu$ and $\Lambda^- = \frac{1}{2}$ we recover a very similar version of REG, which we label as "symmetrized" REG (S-REG). For example, in $d2Q9$, the only difference is identified in the fourth-order moment relaxation s_ε^+, which is $s_\varepsilon^+ = 1$ (fixed) in original REG while $s_\varepsilon^+ = 1/\tau$ (viscosity dependent) in S-REG. Yet, as pointed out before for MRT, the higher-order symmetric modes, and particularly ε mode, appear to play a negligible impact on the simulations of microchannel fluid flows and this was confirmed by our numerical tests. Hence, for the purpose of this study, REG and S-REG are virtually equivalent (with the advantage of the latter exhibiting a more convenient computational implementation and a simpler structure for theoretical analyses).

BGK: The single relaxation time (BGK) collision operator [36,37,71] is the simplest relaxing setting in LBM. Here, all collision modes are controlled by a single relaxation parameter τ, which simultaneously determines the fluid viscosity as $\nu = \frac{1}{3}(\tau - \frac{1}{2})$ and the spatial truncation errors as $\propto \nu^2$ [73]. This last point is the principal source of shortcomings identified in the performance of BGK [73]. Evidently, the BGK is a subclass of other collision operators. Namely, BGK is recovered by (i) MRT with $s_k = 1/\tau$ with $k = 1, \ldots, Q$; (ii) TRT with $\Lambda^+ = \Lambda^- = (\tau - \frac{1}{2})$; and (iii) REG (or S-REG) with $\tau = 1$.

APPENDIX B: RECOVERING DBB SCHEME IN [56]

This Appendix elaborates on the equivalence between the DBB solutions for the calibration of r and Λ, summarized in Tables III and IV, and the corresponding solutions derived in [56], specifically Eq. (29) of [56]. The interest in showing this equality comes from the different theoretical frameworks adopted by each work. While we operate on the basis of the second-order Chapman-Enskog expansion, as popularized by multireflection works [63,64,67,94,97,112], the study [56] develops on the much more hardworking procedure of [122]. The common point is that the two cases rely on a lattice-aligned channel flow for carrying out the derivations, although we note that [56] considers further constraints, which are detailed below.

Let us start out by recalling the solutions of r and Λ of DBB, given in Tables III and IV of Sec. IV, namely,

$$r = \frac{(3\nu - C_1\lambda_\Theta) - (\delta_{y'} - 1/2)}{(3\nu + C_1\lambda_\Theta) + (\delta_{y'} - 1/2)}, \tag{B1a}$$

$$\Lambda = \frac{3\Theta^2}{3\Theta - 1}\left[\frac{1}{2}\left(\delta_{y'}^2 - \delta_{y'} + \frac{1}{2}\right) + C_1\lambda_\Theta\left(\delta_{y'} - \frac{1}{2}\right) + C_2\lambda_\Theta^2\right]. \tag{B1b}$$

Now, let us adopt [56] notation and replace $\delta_{y'}$ by Δ following the transformation $\Delta = (1 - \delta_{y'})$. Moreover, let us introduce the two extra assumptions used by [56], namely, (i) horizontal channel $\Theta = 1$, and (ii) viscosity and mean-free-path relationship $\nu = \overline{\xi}\lambda$ with $\overline{\xi} = \frac{1}{3}\sqrt{\frac{6}{\pi}}$. Finally, let us introduce the specific MRT notation used by [56] for the relaxation parameters: $\nu = \frac{1}{3}(\tau_s - \frac{1}{2})$ and $\Lambda = (\tau_s - \frac{1}{2})(\tau_q - \frac{1}{2})$. With these changes, our Eq. (B1) rewrites as follows:

$$r = \frac{\left(\tau_s - \frac{1}{2}\right)\left(1 - C_1\sqrt{\frac{\pi}{6}}\right) - \left(\frac{1}{2} - \Delta\right)}{\left(\tau_s - \frac{1}{2}\right)\left(1 + C_1\sqrt{\frac{\pi}{6}}\right) + \left(\frac{1}{2} - \Delta\right)}, \tag{B2a}$$

$$\begin{aligned}\left(\tau_s - \tfrac{1}{2}\right)\left(\tau_q - \tfrac{1}{2}\right) &= \tfrac{3}{2}\Big[\tfrac{1}{2}\left(\Delta^2 - \Delta + \tfrac{1}{2}\right) + \left(\tau_s - \tfrac{1}{2}\right)\sqrt{\tfrac{\pi}{6}}C_1\left(\tfrac{1}{2} - \Delta\right) \\ &\quad + \left(\tau_s - \tfrac{1}{2}\right)^2\tfrac{\pi}{6}C_2\Big].\end{aligned} \tag{B2b}$$

Equation (B2) can be further simplified to

$$r = \frac{\left(\frac{1}{2} - \tau_s\right)C_1 + (\tau_s + \Delta - 1)\sqrt{\frac{6}{\pi}}}{\left(\tau_s - \frac{1}{2}\right)C_1 + (\tau_s - \Delta)\sqrt{\frac{6}{\pi}}} \tag{B3a}$$

$$\begin{aligned}\left(\tau_q - \tfrac{1}{2}\right) &= \tfrac{3}{4}\frac{1}{\left(\tau_s - \frac{1}{2}\right)}\left(\Delta^2 - \Delta + \tfrac{1}{2}\right) \\ &\quad + \tfrac{3}{2}\sqrt{\tfrac{\pi}{6}}C_1\left(\tfrac{1}{2} - \Delta\right) + \tfrac{3}{2}\tfrac{\pi}{6}C_2\left(\tau_s - \tfrac{1}{2}\right).\end{aligned} \tag{B3b}$$

Finally, we solve Eq. (B3a) for C_1, which yields $C_1 = \sqrt{\frac{6}{\pi}}[2\Delta - 1 + (r-1)(\Delta - \tau_s)]/[(1+r)(\tau_s - \frac{1}{2})]$. Then, after substituting the C_1 expression into Eq (B3b), we recover the r and τ_q solutions as given by Eq. (29) of [56]:

$$r = \frac{\left(\frac{1}{2} - \tau_s\right)C_1 + (\tau_s + \Delta - 1)\sqrt{\frac{6}{\pi}}}{\left(\tau_s - \frac{1}{2}\right)C_1 + (\tau_s - \Delta)\sqrt{\frac{6}{\pi}}} \tag{B4a}$$

$$\begin{aligned}\tau_q &= \frac{(6\Delta - 1)\tau_s r + (5 - 6\Delta)\tau_s + \left(\frac{1}{2} - 3\Delta^2\right)r - 3\Delta^2 + 6\Delta - \frac{5}{2}}{4(r+1)\left(\tau_s - \frac{1}{2}\right)} \\ &\quad + \tfrac{\pi}{4}C_2\left(\tau_s - \tfrac{1}{2}\right).\end{aligned} \tag{B4b}$$

This proves that [56] can be recovered as a particular solution of the general framework developed in Sec. IV.

[1] G. K. Batchelor, *An Introduction to Fluid Dynamics*, Cambridge Mathematical Library (Cambridge University Press, Cambridge, 2000).

[2] C. Cercignani, *The Boltzmann Equation and Its Application* (Springer, New York, 1988).

[3] I. N. Ivchenko, S. K. Loyalka, and R. V. Tompson, Jr., *Analytical Methods for Problems of Molecular Transport* (Springer, Dordrecht, 2007).

[4] M. N. Kogan, *Rarefied Gas Dynamics* (Plenum, New York, 1969).

[5] G. E. Uhlenbeck and G. W. Ford, *Lectures in Statistical Mechanics* (American Mathematical Society, Providence, RI, 1963).

[6] C.-M. Ho and Y.-C. Tai, Micro-electro-mechanical systems (MEMS) and fluid flows, Annu. Rev. Fluid Mech. **30**, 579 (1988).

[7] M. Gad-el-Hak, The fluid mechanics of microdevices: The freeman scholar lecture, J. Fluids Eng. **121**, 5 (1999).

[8] H. A. Stone, A. D. Stroock, and A. Ajdari, Engineering flows in small devices: Microfluidics toward a laboratory-on-a-chip, Annu. Rev. Fluid Mech. **36**, 381 (2004).

[9] J. Zengerle, R. Newman, J. Ernst, H. Riedmüller, K. Messner, S. Andrieux, G. Provence, M. Eloy, and J. C. Ducrée, *FlowMap: Microfluidics Roadmap for the Life Sciences* (Books on Demand, GmbH, 2004).

[10] P. Abgrall and N.-T. Nguyen, *Nanofluidics* (Artech House, Norwood, MA, 2009).

[11] F. Sharipov and V. Seleznev, Data on internal rarefied gas flows, J. Phys. Chem. Ref. Data **27**, 657 (1998).

[12] N. G. Hadjiconstantinou, The limits of Navier-Stokes theory and kinetic extensions for describing small-scale gaseous hydrodynamics, Phys. Fluids **18**, 111301 (2006).

[13] G. H. Tang, Y. L. He, and Q. Tao, Comparison of gas slip models with solutions of linearized Boltzmann equation and direct simulation of Monte Carlo method, Int. J. Mod. Phys. C **18**, 203 (2007).

[14] W.-M. Zhang, G. Meng, and X. Wei, A review on slip models for gas microflows, Microfluid. Nanofluid. **13**, 845 (2012).

[15] J. C. Maxwell, On stresses in rarefied gases arising from inequalities of temperature, Philos. Trans. R. Soc. London **170**, 231 (1879).

[16] D. Einzel, P. Panzer, and M. Liu, Boundary Condition for Fluid Flow: Curved or Rough Surfaces, Phys. Rev. Lett. **64**, 2269 (1990).

[17] K. W. Tibbs, F. Baras, and A. L. Garcia, Anomalous flow profile due to the curvature effect on slip length, Phys. Rev. E **56**, 2282 (1997).

[18] R. W. Barber, Y. Sun, X. J. Gu, and D. R. Emerson, Isothermal slip flow over curved surfaces, Vacuum **76**, 73 (2004).

[19] L. Wu, A slip model for rarefied gas flows at arbitrary Knudsen number, Appl. Phys. Lett. **93**, 253103 (2008).

[20] S. Wang, A. A. Lukyanov, L. Wang, Y.-S. Wu, A. Pomerantz, W. Xu, and R. Kleinberg, A non-empirical gas slippage model for low to moderate Knudsen numbers, Phys. Fluids **29**, 012004 (2017).

[21] C. Cercignani, *Mathematical Methods in Kinetic Theory* (Plenum, New York, 1990).

[22] N. G. Hadjiconstantinou, Comment on Cercignani's second-order coefficient, Phys. Fluids **15**, 2352 (2003).
[23] D. A. Lockerby, J. M. Reese, D. R. Emerson, and R. W. Barber, Velocity boundary condition at solid walls in rarefied gas calculations, Phys. Rev. E **70**, 017303 (2004).
[24] H. Struchtrup and M. Torrilhon, Higher-order effects in rarefied channel flows, Phys. Rev. E **78**, 046301 (2008).
[25] C. L. M. H. Navier, Mémoire sur les lois du mouvement des fluides, Mem. Acad. R. Sci. Inst. France **6**, 389 (1823).
[26] G. A. Bird, *Molecular Gas Dynamics and the Direct Simulation of Gas Flows* (Clarendon Press, Oxford, 1994).
[27] A. Sunarso, T. Yamamoto, and N. Mori, Numerical analysis of wall slip effects on flow of Newtonian and Non-Newtonian fluids in macro and micro contraction channels, J. Fluids Eng. **129**, 23 (2007).
[28] L. Ferras, J. M. Nobrega, and F. Pinho, Implementation of slip boundary conditions in the finite volume method: New techniques, Int. J. Numer. Meth. Fluids **72**, 724 (2013).
[29] C. S. Chen, S. M. Lee, and J. D. Sheu, Numerical analysis of gas flow in microchannels, Numer. Heat Transfer, Part A **33**, 749 (1998).
[30] H. Zhao, The numerical solution of gaseous slip flows in microtubes, Int. Commun. Heat Mass Transfer **28**, 585 (2001).
[31] S. Roy, R. Raju, H. F. Chuang, B. A. Cruden, and M. Meyyappan, Modeling gas flow through microchannels and nanopores, J. Appl. Phys. **93**, 4870 (2003).
[32] R. Raju and S. Roy, Hydrodynamic study of high speed flow and heat transfer through microchannel, J. Thermophys. Heat Transfer **19**, 106 (2005).
[33] J. M. Urquiza, A. Garon, and M.-I. Farinas, Weak imposition of the slip boundary condition on curved boundaries for Stokes flow, J. Comput. Phys. **256**, 748 (2014).
[34] A. Beskok and G. E. Karniadakis, A model for flows in channels, pipes, and ducts at micro and nano scales, Microscale Thermophys. Eng. **3**, 43 (1999).
[35] G. E. Karniadakis and A. Beskok, *Micro Flow: Fundamentals and Simulation* (Springer, New York, 2001).
[36] S. Succi, *The Lattice Boltzmann Equation for Fluid Dynamics and Beyond* (Oxford University Press, Oxford, 2001).
[37] T. Krüger, H. Kusumaatmaja, A. Kuzmin, O. Shardt, G. Silva, and E. M. Viggen, *The Lattice Boltzmann Method: Principles and Practice* (Springer, Berlin, 2016).
[38] S. Chen and G. D. Doolen, Lattice Boltzmann method for fluid flows, Annu. Rev. Fluid Mech. **30**, 329 (1998).
[39] C. K. Aidun and J. R. Clausen, Lattice-Boltzmann method for complex flows, Annu. Rev. Fluid Mech. **42**, 439 (2010).
[40] X. Shan, X.-F. Yuan, and H. Chen, Kinetic theory representation of hydrodynamics: A way beyond the Navier-Stokes equation, J. Fluid Mech. **550**, 413 (2006).
[41] J. Zhang, Lattice Boltzmann method for microfluidics: Models and applications, Microfluid. Nanofluid. **10**, 1 (2010).
[42] J. Meng and Y. Zhang, Accuracy analysis of high-order lattice Boltzmann models for rarefied gas flows, J. Comput. Phys. **230**, 835 (2011).
[43] V. Ambrus and V. Sofonea, Lattice Boltzmann models based on half-range Gauss–Hermite quadratures, J. Comput. Phys. **316**, 760 (2016).
[44] C. Feuchter and W. Schleifenbaum, High-order lattice Boltzmann models for wall-bounded flows at finite Knudsen numbers, Phys. Rev. E **94**, 013304 (2016).
[45] S. Succi, Mesoscopic Modeling of Slip Motion at Fluid-Solid Interfaces with Heterogeneous Catalysis, Phys. Rev. Lett. **89**, 064502 (2002).
[46] G. H. Tang, W. Q. Tao, and Y. L. He, Lattice Boltzmann method for simulating gas flow in microchannels, Int. J. Mod. Phys. C **15**, 335 (2004).
[47] M. Sbragaglia and S. Succi, Analytical calculation of slip flow in lattice Boltzmann models with kinetic boundary conditions, Phys. Fluids **17**, 093602 (2005).
[48] L. Szalmas, Slip-flow boundary condition for straight walls in the lattice Boltzmann model, Phys. Rev. E **73**, 066710 (2006).
[49] Z. Guo, B. Shi, T. S. Zhao, and C. Zheng, Discrete effects on boundary conditions for the lattice Boltzmann equation in simulating microscale gas flows, Phys. Rev. E **76**, 056704 (2007).
[50] Z. Guo and C. Zheng, Analysis of lattice Boltzmann equation for microscale gas flows: Relaxation time, Boundary condition, and Knudsen layer, Int. J. Comput. Fluid Dyn. **22**, 465 (2008).
[51] F. Verhaeghe, L.-S. Luo, and B. Blanpain, Lattice Boltzmann modeling of microchannel flow in slip flow regime, J. Comput. Phys. **228**, 147 (2009).
[52] Z. Chai, Z. Guo, L. Zheng, and B. Shi, Lattice Boltzmann simulation of surface roughness effect on gaseous flow in microchannel, J. Appl. Phys. **104**, 014902 (2008).
[53] Z. Chai, B. Shi, Z. Guo, and J. Lu, Gas flow through square arrays of circular cylinders with Klinkenberg effect: A lattice Boltzmann study, Commun. Comput. Phys. **8**, 1052 (2010).
[54] S. H. Kim, H. Pitsch, and I. D. Boyd, Slip velocity and Knudsen layer in lattice Boltzmann method for microscale flows, Phys. Rev. E **77**, 026704 (2008).
[55] Z. Guo, B. Shi, and C. Zheng, Velocity inversion of micro cylindrical Couette flow: A lattice Boltzmann study, Comput. Math. Appl. **61**, 3519 (2011).
[56] S. Tao and Z. Guo, Boundary condition for lattice Boltzmann modeling of microscale gas flows with curved walls in the slip regime, Phys. Rev. E **91**, 043305 (2015).
[57] T. Reis and P. J. Dellar, Lattice Boltzmann simulations of pressure-driven flows in microchannels using Navier-Maxwell slip boundary conditions, Phys. Fluids **24**, 112001 (2012).
[58] X. He and L.-S. Luo, Theory of the lattice Boltzmann method: From the Boltzmann equation to the lattice Boltzmann equation, Phys. Rev. E **56**, 6811 (1997).
[59] X. Shan and X. He, Discretization of the Velocity Space in the Solution of the Boltzmann Equation, Phys. Rev. Lett. **80**, 65 (1998).
[60] S. Ansumali and I. V. Karlin, Kinetic boundary conditions in the lattice Boltzmann method, Phys. Rev. E **66**, 026311 (2002).
[61] W. H. Yudistiawan, S. Ansumali, and I. V. Karlin, Hydrodynamics beyond Navier-Stokes: The slip flow model, Phys. Rev. E **78**, 016705 (2008).
[62] Z. Guo, C. Zheng, and B. Shi, Lattice Boltzmann with multiple effective relation times for gaseous microscale flows, Phys. Rev. E **77**, 036707 (2008).
[63] I. Ginzburg and D. d'Humières, Multi-reflection boundary conditions for lattice Boltzmann models, Phys. Rev. E **68**, 066614 (2003).
[64] I. Ginzburg, F. Verhaeghe, and D. d'Humières, Two-relaxation-times lattice Boltzmann scheme: about paramatrization,

velocity, pressure and mixed boundary conditions, Commun. Comput. Phys. **3**, 427 (2008).

[65] S. Chapman and T. G. Cowling, *The Mathematical Theory of Non-uniform Gases* (Cambridge University Press, Cambridge, 1952).

[66] U. Frisch, D. d'Humières, B. Hasslacher, P. Lallemand, Y. Pomeau, and J.-P. Rivet, Lattice-gas hydrodynamics in two and three dimensions, Complex Syst. **1**, 649 (1987).

[67] I. Ginzburg, F. Verhaeghe, and D. d'Humières, Study of simple hydrodynamic solutions with the two-relaxation-times lattice Boltzmann scheme, Commun. Comput. Phys. **3**, 519 (2008).

[68] I. Ginzburg, L. Roux, and G. Silva, Local boundary reflections in lattice Boltzmann schemes: Spurious boundary layers and their impact on the velocity, diffusion and dispersion, C. R. Mec. **343**, 518 (2015).

[69] I. Ginzburg, Prediction of the moments in advection-diffusion lattice Boltzmann method II Attenuation of the boundary layers via double-Λ bounce-back flux scheme, Phys. Rev. E **95**, 013305 (2017).

[70] F. J. Higuera and J. Jiménez, Boltzmann approach to lattice gas simulations, Europhys. Lett. **9**, 663 (1989).

[71] Y. H. Qian, D. d'Humiéres, and P. Lallemand, Lattice BGK models for Navier-Stokes equation, Europhys. Lett. **17**, 479 (1992).

[72] D. d'Humières, Generalized lattice Boltzmann equations, in *Rarefied Gas Dynamics: Theory and Simulations*, edited by B. Shizgal and D. Weaver (AIAA, Reston, VA, 1992), Vol. 159, pp. 450–458.

[73] D. d'Humières and I. Ginzburg, Viscosity independent numerical errors for Lattice Boltzmann models: From recurrence equations to "magic" collision numbers, Comput. Math. Appl. **58**, 823 (2009).

[74] X. He and L.-S. Luo, Lattice Boltzmann model for the incompressible Navier-Stokes equation, J. Stat. Phys. **88**, 927 (1997).

[75] P. Lallemand and L.-S. Luo, Theory of the lattice Boltzmann method: Dispersion, dissipation, isotropy, Galilean invariance, and stability, Phys. Rev. E **61**, 6546 (2000).

[76] I. Ginzburg, Truncation errors, exact and heuristic stability analysis of two-relaxation-times lattice boltzmann schemes for anisotropic advection-diffusion equation, Commun. Comput. Phys. **11**, 1439 (2012).

[77] J. M. Buick and C. A. Greated, Gravity in a lattice Boltzmann model, Phys. Rev. E **61**, 5307 (2000).

[78] G. Silva and V. Semiao, A study on the inclusion of body forces in the lattice Boltzmann BGK equation to recover steady-state hydrodynamics, Phys. A (Amsterdam) **390**, 1085 (2011).

[79] G. Silva and V. Semiao, First- and second-order forcing expansions in a lattice Boltzmann method reproducing isothermal hydrodynamics in artificial compressibility form, J. Fluid Mech. **698**, 282 (2012).

[80] K. Suga, Lattice Boltzmann method for complex microflows: Applicability and limitations for practical applications, Fluid Dyn. Res. **45**, 034501 (2013).

[81] H. Chen, R. Zhang, I. Staroselsky, and M. Jhon, Recovery of full rotational invariance in lattice Boltzmann formulations for high Knudsen number flows, Phys. A (Amsterdam) **362**, 125 (2005).

[82] R. Zhang, X. Shan, and H. Chen, Efficient kinetic method for fluid simulation beyond the Navier-Stokes, Phys. Rev. E **74**, 046703 (2006).

[83] X.-D. Niu, S.-A. Hyodo, T. Munekata, and K. Suga, Kinetic lattice Boltzmann method for microscale gas flow: Issues on boundary condition, relaxation time, and regularization, Phys. Rev. E **76**, 036711 (2007).

[84] C. E. Colosqui, H. Chen, X. Shan, and V. Yakhot, Propagating high frequency shear waves in simple fluids, Phys. Fluids **21**, 013105 (2009).

[85] C. E. Colosqui, High-order Hydrodynamics via lattice Boltzmann methods, Phys. Rev. E **81**, 026702 (2010).

[86] K. Suga, S. Takenaka, T. Ito, M. Kaneda, T. Kinjo, and S. Hyodo, Evaluation of a lattice Boltzmann method in a complex nanoflow, Phys. Rev. E **82**, 016701 (2010).

[87] A. Montessori, P. Prestininzi, M. La Rooca, and S. Succi, Lattice Boltzmann approach for complex nonequilibrium flows, Phys. Rev. E **92**, 043308 (2015).

[88] X. Nie, G. D. Doolen, and S. Chen, Lattice-Boltzmann simulations of fluid flows in MEMS, J. Stat. Phys. **107**, 279 (2002).

[89] B. Li and D. Kwok, Discrete Boltzmann Equation for Microfluidics, Phys. Rev. Lett. **90**, 124502 (2003).

[90] C. Shen, D. B. Tian, C. Xie, and J. Fan, Examination of the LBM in simulation of microchannel flow in transitional regime, Microscale Thermophys. Eng. **8**, 423 (2004).

[91] F. Toschi and S. Succi, Lattice Boltzmann method at finite-Knudsen number, Europhys. Lett. **69**, 549 (2005).

[92] J. Latt and B. Chopard, Lattice Boltzmann method with regularized pre-collision distribution functions, Math. Comput. Simul. **72**, 165 (2006).

[93] I. Ginzburg, Consistent lattice Boltzmann schemes for the Brinkman model of porous flow and infinite Chapman-Enskog expansion, Phys. Rev. E **77**, 066704 (2008).

[94] S. Khirevich, I. Ginzburg, and U. Tallarek, Coarse- and fine-grid numerical behavior of MRT/TRT lattice-Boltzmann schemes in regular and random sphere packings, J. Comput. Phys. **281**, 708 (2015).

[95] N. G. Hadjiconstantinou, Validation of a second-order slip model for dilute gas flows, Microscale Thermophys. Eng. **9**, 137 (2005).

[96] D. A. Lockerby and J. M. Reese, On the modeling of isothermal gas flows at the microscale, J. Fluid Mech. **604**, 235 (2008).

[97] I. Ginzbourg and D. d'Humières, Local second-order boundary methods for lattice Boltzmann models, J. Stat. Phys. **84**, 927 (1996).

[98] M. Bouzidi, M. Firdaouss, and P. Lallemand, Momentum transfer of a Boltzmann-lattice fluid with boundaries, Phys. Fluids **13**, 3452 (2001).

[99] D. Yu, R. Mei, L.-S. Luo, and W. Shyy, Viscous flow computations with the method of lattice Boltzmann equation, Prog. Aerosp. Sci. **39**, 329 (2003).

[100] B. Chun and A. J. C. Ladd, Interpolated boundary condition for lattice Boltzmann simulations of flows in narrow gaps, Phys. Rev. E **75**, 066705 (2007).

[101] A. Norouzi and J. A. Esfahani, Two relaxation time lattice Boltzmann equation for high Knudsen number flows using wall function approach, Microfluid. Nanofluid. **18**, 323 (2014).

[102] P. Prestininzi, A. Montessori, and S. Succi, Reassing the single relaxation time Lattice Boltzmann Method for the simulation of Darcy's flows, Int. J. Mod. Phys. C **27**, 1650037 (2016).

[103] R. Cornubert, D. d'Humiéres, and D. Levermore, A Knudsen layer theory for lattice Gases, Phys. D (Amsterdam) **47**, 241 (1991).

[104] I. Ginzburg and K. Steiner, Lattice Boltzmann model for free-surface flow and its application to filling process in casting, J. Comput. Phys. **185**, 61 (2003).

[105] G. H. Tang, W. Q. Tao, and Y. L. He, Lattice Boltzmann method for gaseous microflows using kinetic theory boundary conditions, Phys. Fluids **17**, 058101 (2005).

[106] S. Ansumali, I. V. Karlin, C. E. Frouzakis, and K. B. Boulouchos, Entropic lattice Boltzmann method for microflows, Phys. A (Amsterdam) **359**, 289 (2006).

[107] S. H. Kim, H. Pitsch, and I. D. Boyd, Accuracy of higher-order lattice Boltzmann mmethod for microscale flows with finite Knudsen numbers, J. Comput. Phys. **227**, 8655 (2008).

[108] C. Y. Lim, C. Shu, X. D. Niu, and Y. T. Chew, Application of lattice Boltzmann method to simulate microchannel flows, Phys. Fluids **14**, 2299 (2002).

[109] T. Lee and C. L. Lin, Rarefaction and compressibility of the lattice Boltzmann equation method in a gas microchannel, Phys. Rev. E **71**, 046706 (2005).

[110] Y. H. Zhang, R. Qin, and D. R. Emerson, Lattice Boltzmann simulation of rarefied gas flows in microchannels, Phys. Rev. E **71**, 047702 (2005).

[111] Z. L. Guo, T. S. Zhao, and Y. Shi, Physical symmetry, spatial accuracy and relaxation time of the lattice Boltzmann equation for micro gas flows, J. Appl. Phys. **99**, 074903 (2006).

[112] I. Ginzbourg and P. M. Adler, Boundary flow condition analysis for the three-dimensional lattice Boltzmann model, J. Phys. (France) **4**, 191 (1994).

[113] G. Silva, L. Talon, and I. Ginzburg, Low- and high-order accurate boundary conditions: From Stokes to Darcy porous flow modeled with standard and improved Brinkman lattice Boltzmann schemes, J. Comput. Phys. **335**, 50 (2017).

[114] B. Li and D. Y. Kwok, Reply to "Comment on Discrete Boltzmann Equation for Microfluidics," Phys. Rev. Lett. **92**, 139402 (2004).

[115] L.-S. Luo, Comment on "Discrete Boltzmann Equation for Microfluidics," Phys. Rev. Lett. **92**, 139401 (2004).

[116] L.-S. Luo, W. Liao, X. Chen, Y. Peng, and W. Zhang, Numerics of the lattice Boltzmann method: Effects of collision models on the lattice Boltzmann simulations, Phys. Rev. E **83**, 056710 (2011).

[117] L.-S. Luo, Comment on Heat transfer and fluid flow in microchannels and nanochannels at high Knudsen number using thermal lattice-Boltzmann method, Phys. Rev. E **84**, 048301 (2011).

[118] A. J. C. Ladd, Numerical simulations of particulate suspensions via a discretized Boltzmann equation. Part 1. Theoretical foundation, J. Fluid Mech. **271**, 285 (1994).

[119] A. J. C. Ladd, Numerical simulations of particulate suspensions via a discretized Boltzmann equation. Part 2. Numerical results, J. Fluid Mech. **271**, 311 (1994).

[120] C. Pan, L.-S. Luo, and C. T. Miller, An evaluation of lattice Boltzmann schemes for porous medium flow simulation, Comput. Fluids **35**, 898 (2006).

[121] M. C. Sukop and D. T. Thorne, *Lattice Boltzmann Modeling An Introduction for Geoscientists and Engineers* (Springer, New York, 2006).

[122] X. He, Q. Zou, L.-S. Luo, and M. Dembo, Analytical solutions of simple flows and analysis of nonslip boundary conditions for the lattice Boltzmann BGK model, J. Stat. Phys. **87**, 115 (1997).

[123] I. Ginzburg, Prediction of the moments in advection-diffusion lattice Boltzmann method. I. Truncation dispersion, skewness, and kurtosis, Phys. Rev. E **95**, 013304 (2017).

[124] I. Ginzburg, G. Silva, and L. Talon, Analysis and improvement of Brinkman lattice Boltzmann schemes: Bulk, boundary, interface. Similarity and distinctness with finite elements in heterogeneous porous media, Phys. Rev. E **91**, 023307 (2015).

[125] L. Talon, D. Bauer, N. Gland, S. Youssef, H. Auradou, and I. Ginzburg, Assessment of the two relaxation time Lattice-Boltzmann scheme to simulate Stokes flow in porous media, Water Resour. Res. **48**, W04526 (2012).

[126] I. Ginzburg, Multiple anisotropic ccollision for advection-diffusion lattice Boltzmann schemes, Adv. Water Res. **51**, 381 (2013).

[127] R. Adhikari and S. Succi, Duality in matrix lattice Boltzmann models, Phys. Rev. E **78**, 066701 (2008).

[128] A. Montessori, G. Falcucci, P. Prestininzi, M. La Rocca, and S. Succi, Regularized lattice Bhatnagar-Gross-Krook model for two- and three-dimensional cavity flow simulations, Phys. Rev. E **89**, 053317 (2014).